

Transition in boundary layers subject to free-stream turbulence

By LUCA BRANDT¹, PHILIPP SCHLATTER²
AND DAN S. HENNINGSON^{1,3}

¹KTH Mechanics, S-100 44 Stockholm, Sweden

²Institute of Fluid Dynamics, Swiss Federal Institute of Technology (ETH),
CH-8092 Zürich, Switzerland

³FOI, The Swedish Defense Research Agency, Aeronautics Division,
SE-17290 Stockholm, Sweden

(Received 3 September 2003 and in revised form 24 June 2004)

The effect of high levels of free-stream turbulence on the transition in a Blasius boundary layer is studied by means of direct numerical simulations, where a synthetic turbulent inflow is obtained as superposition of modes of the continuous spectrum of the Orr–Sommerfeld and Squire operators. In the present bypass scenario the flow in the boundary layer develops streamwise elongated regions of high and low streamwise velocity and it is suggested that the breakdown into turbulent spots is related to local instabilities of the strong shear layers associated with these streaks. Flow structures typical of the spot precursors are presented and these show important similarities with the flow structures observed in previous studies on the secondary instability and breakdown of steady symmetric streaks.

Numerical experiments are performed by varying the energy spectrum of the incoming perturbation. It is shown that the transition location moves to lower Reynolds numbers by increasing the integral length scale of the free-stream turbulence. The receptivity to free-stream turbulence is also analysed and it is found that two distinct physical mechanisms are active depending on the energy content of the external disturbance. If low-frequency modes diffuse into the boundary layer, presumably at the leading edge, the streaks are induced by streamwise vorticity through the linear lift-up effect. If, conversely, the free-stream perturbations are mainly located above the boundary layer a nonlinear process is needed to create streamwise vortices inside the shear layer. The relevance of the two mechanisms is discussed.

1. Introduction

1.1. *Aim of the present work*

In boundary layers with free-stream turbulence intensities of 1% or more, transition occurs rapidly, bypassing the classical scenario triggered by the viscous, thus slower, exponential amplification of unstable waves (the Tollmien–Schlichting (TS) waves). The former scenario, denoted bypass transition, is characterized by the appearance inside the boundary layer of streamwise elongated streaky structures of alternating high and low streamwise velocity. As the streaks grow downstream, they undergo wavy motions which precede the breakdown into regions of intense randomized flow, turbulent spots. The spots grow in size and merge until the flow is fully turbulent.

The overall picture of the transition scenario has been elucidated by flow visualizations and velocity measurements in previous experimental studies (see the review

articles by Kendall 1998; Matsubara & Alfredsson 2001; Saric, Reed & Kerschen 2002). However, some important points still remain unclear: these concern mainly the receptivity stage, during which perturbations enter the boundary layer, and the mechanisms of the breakdown into turbulent spots occurring on isolated streaks. To answer these questions, we present here extensive numerical simulations of transition in a Blasius boundary layer subjected to free-stream turbulence, where the turbulent inflow is generated by the superposition of modes of the continuous spectrum of the Orr–Sommerfeld and Squire operators. The simulation of a fully transitional boundary layer is a formidable task even for the modern supercomputers and therefore we cannot hope to reproduce as rich parametric studies as in experimental works. However, it is possible to reproduce correctly the main features of the transition scenario under consideration (see Jacobs & Durbin 2001) and, as a consequence, simulations can be designed to investigate specific problems, thus exploiting the advantages of a numerical study. This enabled us to identify the relevant flow structures at the breakdown, which is not possible in an experiment owing to the random nature of the spot appearance. Moreover, the numerical methodology used allows us to determine and manipulate the energy content of the turbulent inflow. In this way, it has been possible to investigate the receptivity mechanism and the effect of the characteristic length scale of the free-stream turbulence.

1.2. Previous experimental and numerical work

The occurrence of streamwise elongated structures in boundary layers subjected to free-stream turbulence was first identified by Klebanoff (1971) in terms of low-frequency oscillations in hot-wire signals caused by the slow spanwise motions of the streaks, although the first experimental results on boundary-layer disturbances under free-stream turbulence date back to Dryden (1937) and Taylor (1939). Arnal & Juillen (1978) also showed that for free-stream turbulence levels higher than 0.5–1%, the dominant disturbances inside the boundary layer are characterized by low frequencies and they are not TS-waves. Kendall (1985) denoted these disturbances as Klebanoff modes.

The detailed measurements of a zero-pressure-gradient boundary layer subject to free-stream turbulence by Westin *et al.* (1994) confirmed that the amplitude of the streamwise velocity perturbation increases as the square root of the distance from the leading edge. Further, these authors compiled data from different studies and observed that different experiments with apparently similar conditions can disagree on the onset and extent of transition. In fact, a number of different parameters affect the receptivity of the boundary layer; not only the free-stream turbulence intensity, but also its spatial scales, energy spectrum and degree of isotropy and homogeneity play an important role. A complete description of disturbance growth in boundary layers disturbed by free-stream turbulence can be found in Matsubara & Alfredsson (2001), where several years of experiments performed at the Royal Institute of Technology, in Stockholm are reviewed. In the above, it is concluded that the initial growth of the streaks can be successfully explained by theories of non-modal or transient growth. These authors also show that the spanwise scale of the streaks decrease downstream, approaching the value of the boundary-layer thickness and that the streak length grows as the boundary-layer thickness (see also Lundell & Alfredsson 2004).

The first direct numerical simulation (DNS) of transition in a boundary layer subjected to free-stream turbulence was attempted by Rai & Moin (1993). In that case, the computational inlet was located upstream of a sharp leading edge, which imposed heavy computational requirements. Probably because of these limitations, the values of the skin-friction coefficient were found to be sensitive to grid resolution,

reaching values well above those typical of turbulent boundary layers. Yang & Voke (1995) performed large-eddy simulations of a boundary layer under free-stream turbulence and indicated the key influence of the wall-normal component of the outside perturbation in provoking transition. Wu *et al.* (1999) presented DNS of boundary-layer transition beneath periodic passing wakes. In this case, long streaks are precluded by the finite width of the wake; however, the breakdown into turbulent spots is still associated to low-speed regions ('backward jets') located in the upper part of the boundary layer.

Direct numerical simulations of a boundary layer disturbed by free-stream turbulence were performed by Jacobs & Durbin (2001). Implementing the methodology first proposed by Grosch & Salwen (1978), these authors constructed a turbulent inflow by expanding the free-stream turbulence as a sum of spanwise and temporal Fourier modes, multiplied by wall-normal Orr–Sommerfeld modes. The latter consisted of modes of the continuous spectrum, which can be considered a natural basis for free-stream turbulence since they have a sinusoidal behaviour far above the boundary layer and vanish inside. Such an inflow is applied a short distance downstream of the leading edge and the results obtained are in good agreement with the laboratory measurements by Roach & Brierley (1990). Jacobs & Durbin (2001) show that streaks are formed by penetration of low-frequency modes from the free stream. The perturbation spectrum evolves from the synthetic inflow into a different spectrum dominated by low frequencies through nonlinear effects. These authors also observed that spot precursors are localized instabilities of single low-speed streaks and suggest that the breakdown of these structures is forced by the interaction between streaks and small scales in the free stream.

1.3. Non-modal disturbance growth and receptivity

From a theoretical point of view, a disturbance growth mechanism alternative to Tollmien–Schlichting waves is required to explain transition observed in flows at Reynolds numbers well below the critical ones from linear stability theory, as well as the different features of the structures observed.

Ellingsen & Palm (1975) proposed a growth mechanism, considering the linear inviscid evolution of an initial disturbance independent of the streamwise coordinate in a shear layer. These authors showed that the streamwise velocity component may grow linearly in time, producing alternating low- and high-velocity streaks. Moffat also identified such a streak growth mechanism in a model of turbulent uniform shear flow (see the review article by Phillips 1969). Later Hultgren & Gustavsson (1981) considered the temporal evolution of a three-dimensional disturbance in a boundary layer and found that in a viscous flow the initial growth is followed by a viscous decay (transient growth).

Landahl (1975, 1980) studied the linear evolution of localized disturbances and formalized a physical explanation for the streak growth mechanism, which we denote the lift-up effect. Since a fluid particle in a streamwise vortex will initially retain its horizontal momentum if displaced in the wall-normal direction, such a disturbance in the wall-normal velocity will cause in a shear layer a perturbation in the streamwise velocity.

It is now understood that since the linearized Navier–Stokes operator is non-normal for many flow cases, a significant transient growth may occur before the subsequent exponential behaviour (Butler & Farrell 1992; Reddy & Henningson 1993; Schmid & Henningson 2001). The class of perturbations which sustain maximum temporal growth in the linear regime takes the form of spanwise periodic streamwise vortices.

Such optimal perturbations give rise to a spanwise periodic distribution of low- and high-speed streaks. This growth is observed also for subcritical values of the Reynolds number and it is the underlying mechanism triggering bypass transition phenomena. The non-normality of the governing operators is associated to the vortex-tilting phenomenon, by which normal vorticity is created by tilting the spanwise vorticity of the basic flow (see Henningson, Lundbladh & Johansson 1993).

To answer the question of which disturbance present at the leading edge gives the largest perturbation in the boundary layer at a certain downstream position, Andersson, Berggren & Henningson (1999) and Luchini (2000) have used an optimization technique adapted from optimal-control theory. The disturbances they found were also streamwise vortices that cause the growth of streaks. These studies show that the energy growth of these optimal perturbations is proportional to the distance to the leading edge x , or alternatively that the streamwise disturbance velocity increases as the square root of x in agreement with the experimental results. Also in remarkable agreement with the experimental findings is the wall-normal shape of the streamwise velocity fluctuations, which is characterized by a maximum in the middle of the boundary layer at $y = 1.3\delta^*$, where δ^* is the local boundary-layer displacement thickness (see Matsubara & Alfredsson 2001). In the theoretical works just mentioned, the spanwise wavenumber β of the disturbance with largest growth at a given streamwise station is found to be $\beta = 0.77/\delta^*$, which corresponds to a spanwise scale approximately 40% larger than the local boundary-layer thickness; this value is slightly larger than that obtained by hot-wire signal correlations. Andersson *et al.* (1999) proposed also a transition prediction criterion which assumes that the Reynolds number at transition onset is inversely proportional to the square of the free-stream turbulence intensity. Although such a criterion is only based on the fact that the linear growth of optimal perturbations is proportional to the square root of the local Reynolds number and it does not consider any of the nonlinear processes occurring at the late stages of the breakdown, it is able to satisfactorily correlate data from several studies (see also Matsubara *et al.* 2000).

Wundrow & Goldstein (2001) and Goldstein & Wundrow (1998) used asymptotic expansions to study the effect of free-stream streamwise vorticity on a laminar boundary layer. Their analysis indicates that the transverse velocity components induce Klebanoff modes inside the boundary layer through a linear mechanism. These authors also show how perturbations of the upstream flow of broadband nature ultimately lead to strong shear layers in certain localized spanwise regions. The theoretical studies discussed so far assumed the presence of perturbations inside the boundary layer or entering it at the leading edge. Herbert & Lin (1993), instead, considered the continuous forcing of Klebanoff modes in a non-parallel boundary layer by using parabolized stability equations. Bertolotti (1997) assumed as initial disturbances vortical modes in the free stream and studied the boundary-layer receptivity in a linear region excluding the leading edge. He has found receptivity to modes with zero streamwise wavenumber, revealing the importance of the forcing generated by the turbulence above the boundary layer. In the following experimental and theoretical study of Bertolotti & Kendall (1997), the external perturbation consisted of a single steady streamwise vortex, created at the tip of a small wing. The agreement between theory and experiments implied that the neglect of the leading-edge region may be justified for very low frequency modes. Westin *et al.* (1998) performed a similar experiment and also emphasized the importance of the continuous influence from the free-stream turbulence along the boundary-layer edge. Elongated low-frequency streamwise vortices can therefore affect the boundary layer both by

entering the boundary layer at the leading edge and by forcing streaks from above all along the plate, with the former mechanism more extensively studied. Berlin & Henningson (1999) have proposed a nonlinear receptivity mechanism by showing how oblique modes in the free stream above the boundary layer can nonlinearly interact to induce strong streaks inside the boundary layer. This nonlinear process has been further investigated in Brandt, Henningson & Ponziani (2002). The relevance of the linear receptivity scenario, assuming the presence of streamwise vortices, and of the nonlinear mechanism is investigated here and it will be the object of one of the sections of this article.

1.4. Streak breakdown

The observation that some streaks develop a streamwise waviness of relatively short wavelength has led to the hypothesis that breakdown to turbulence is caused by a secondary instability developing on the streaks (see Matsubara & Alfredsson 2001). It is known, in fact, that streaky basic flows can undergo exponential inflectional instabilities. The experiments of Swearingen & Blackwelder (1987) were the first to document the emergence of streaks with inflectional profiles due to the formation of Görtler vortices in the boundary layer over a concave wall. This investigation demonstrated that time-dependent fluctuations appear in the flow either in a spanwise symmetric (varicose) or antisymmetric (sinuous) pattern with respect to the underlying streak. The varicose perturbations are more closely related to the wall-normal inflection points whereas the sinuous oscillations are related to the spanwise inflectional profile and they were found to be the fastest growing. The secondary linear instability of Görtler vortices was analysed by Hall & Horseman (1991), Park & Huerre (1995) and Bottaro & Klingmann (1996), whereas the instability of streaks arising from the transient growth of streamwise vortices in channel flows has been studied theoretically by Waleffe (1995, 1997) and Reddy *et al.* (1998) and experimentally by Elofsson, Kawakami & Alfredsson (1999). These studies confirmed that the instability is of inflectional type and that the dominating instability appears as spanwise (sinuous) oscillations of the streaks.

Andersson *et al.* (2001) performed numerical simulations of a zero-pressure-gradient boundary layer to follow the downstream nonlinear saturation of the linear optimal perturbations obtained in Andersson *et al.* (1999). Inviscid secondary instability calculations using Floquet theory were carried out on the basic flows obtained and it was found that the streak critical amplitude, beyond which streamwise travelling waves are excited, is about 26% of the free-stream velocity. The sinuous instability mode (either the fundamental or the subharmonic, depending on the streak amplitude) represents the most dangerous disturbance. Brandt & Henningson (2002) studied the full transition process resulting from the sinuous secondary instability, also through direct numerical simulations. The main structures observed at the late stages of this transition scenario are found to consist of elongated quasi-streamwise vortices located on the flanks of the low-speed streaks, with vortices of alternating sign overlapping in the streamwise direction in a staggered pattern. The widespread occurrence of streaks in various flow configurations has recently led Asai, Minagawa & Nishioka (2002) to examine experimentally the spatial response of a single low-speed streak in a laminar boundary layer submitted to a time-harmonic excitation of sinuous or varicose type. The growth of the sinuous mode was observed to evolve into a train of quasi-streamwise vortices with vorticity of alternate sign. By contrast, the varicose mode led to the formation of hairpin structures made up of a pair of counter-rotating vortices.

The paper is organized as follows. In §2, the numerical method and the turbulent inflow generation procedure are introduced. The results are presented in §3. First, the focus will be on time-averaged data with particular interest in the effect of the integral scale of the outside turbulence. The boundary-layer receptivity is then studied by manipulating the turbulent inflow and by varying the free-stream turbulence intensity and the relevant receptivity mechanisms are discussed. In the last part of §3, the turbulent spot generation is considered. Several spots are traced back in time to the location of their formation so that the relevant flow structures at the breakdown are presented. The paper ends with a summary of the main conclusions.

2. Numerical method

2.1. Numerical scheme

The simulation code (see Lundbladh *et al.* 1999) employed for the present computations uses spectral methods to solve the three-dimensional time-dependent incompressible Navier–Stokes equations over a flat plate. Throughout the paper, the streamwise, wall-normal and spanwise directions are denoted, respectively, by x, y and z and the corresponding velocity components by (u, v, w) . The algorithm uses Fourier representation in the streamwise and spanwise directions and Chebyshev polynomials in the wall-normal direction, together with a pseudo-spectral treatment of the nonlinear terms. The time advancement used is a four-step low-storage third-order Runge–Kutta method for the nonlinear terms and a second-order Crank–Nicolson method for the linear terms. Aliasing errors from the evaluation of the nonlinear terms are removed by the 3/2-rule when the fast Fourier transforms are calculated in the wall-parallel plane. In the wall-normal direction, it has been found more convenient to increase resolution rather than to use dealiasing.

To account for the downstream boundary-layer growth correctly, a spatial technique is necessary. This requirement is combined with the periodic boundary condition in the streamwise direction by the implementation of a ‘fringe region’, similar to that described by Bertolotti, Herbert & Spalart (1992). In this region, at the downstream end of the computational box, the function $\lambda(x)$ in (2.1) is smoothly raised from zero and the flow is forced to a desired solution \mathbf{v} in the following manner,

$$\frac{\partial \mathbf{u}}{\partial t} = NS(\mathbf{u}) + \lambda(x)(\mathbf{v} - \mathbf{u}) + \mathbf{g}, \quad (2.1)$$

$$\nabla \cdot \mathbf{u} = 0, \quad (2.2)$$

where \mathbf{u} is the solution vector and $NS(\mathbf{u})$ the right-hand side of the (unforced) momentum equations. Both \mathbf{g} , which is a disturbance forcing, and \mathbf{v} may depend on the three spatial coordinates and time. The forcing vector \mathbf{v} is smoothly changed from the laminar boundary-layer profile at the beginning of the fringe region to the prescribed inflow velocity vector. This is normally a boundary-layer profile, but can also contain a disturbance.

2.2. Free-stream turbulence generation

The methodology adopted to induce free-stream turbulence at the inlet of the computational domain is similar to that used by Jacobs & Durbin (2001). The turbulent inflow is described as a superposition of modes of the continuous spectrum of the linearized Orr–Sommerfeld and Squire operators. These modes have been added to the forcing vector \mathbf{v} and thus introduced in the fringe region of the numerical code, as described above.

Isotropic grid turbulence can be reproduced by a sum of Fourier modes with random amplitudes (see Rogallo 1981); however, in the presence of an inhomogeneous direction, an alternative complete basis is required; in particular, in the present case, the new basis functions need to accommodate the wall. As pointed out in Grosch & Salwen (1978), a natural choice for the new basis is the use of the modes of the continuous spectrum. These authors showed, in fact, that the Orr–Sommerfeld and Squire eigenvalue problem for a parallel flow in a semi-bounded domain is characterized by a continuous and a discrete spectrum. The discrete mode decay exponentially with the distance from the wall, while modes of the continuous spectrum are sinusoidal in the free stream. As a consequence, by using the second type of mode, a three-dimensional wave-vector $\kappa = (\alpha, \gamma, \beta)$ can be associated to each eigenfunction of the continuous spectrum. Invoking Taylor's hypothesis, the streamwise wavenumber α is replaced by a frequency $\omega = \alpha U_\infty$ in the definition of κ and the expansion is written

$$\mathbf{u} = \sum A_N \hat{\mathbf{u}}_N(y) e^{(i\beta z + i\text{Re}\{\alpha(\omega, \gamma, \beta)\}x - i\omega t)}, \quad (2.3)$$

where the spanwise wavenumber β and ω assume real values and α is a complex eigenvalue of the Orr–Sommerfeld and Squire system for a free stream (see Grosch & Salwen 1978). The streamwise wavenumber α is used in the expression above since the artificial turbulence is forced for the whole length of the fringe region. The desired wall-normal wavenumber γ enters through the eigenfunction shape $\hat{\mathbf{u}}_N(y)$ and it is defined by the specific eigenvalue α picked along the continuous spectrum so that the latter can be computed only if ω, γ and β are known. The modes of the continuous spectrum are all decaying in the streamwise direction ($\text{Im}\{\alpha\} > 0$), with modes of largest γ being the most damped. As a consequence, to avoid forcing very large perturbation velocities at the upstream end of the fringe region we decided to consider only the real part of the eigenvalue α .

In order to obtain isotropic turbulence, several wavenumbers κ have to be selected in the domain $\kappa_l < \kappa < \kappa_u$, where the limiting wavenumbers are determined by the chosen numerical resolution. We divide the wavenumber space (ω, γ, β) into a set of concentric spherical shells (20 in the simulations presented here). Several points are then selected on the surface of each shell and the eigenfunctions of corresponding wavenumbers are included in the summation with an appropriate scaling. From a geometrical point of view, points regularly located on a sphere are defined by the vertices of a regular polyhedron. In particular, a dodecahedron (20 vertices) is considered here. To further increase the degree of isotropy and homogeneity a random three-dimensional rotation is applied to the dodecahedron. By choosing an eigenfunction with wall-normal wavenumber γ , the $-\gamma$ is automatically included in the solution, and a second dodecahedron, symmetric with respect to the (ω, β) -plane, is also considered on each shell. In this way, of the 40 points (terms in the sum) defined on each shell, only the 10 points characterized by positive values of ω and γ need be considered to construct a real-valued superposition.

Once the wavenumbers of the eigenmodes included in the expression (2.3) have been obtained, the values of ω and β are directly known, while the eigenvalue α is computed from the wavenumber γ (see Grosch & Salwen 1978; Jacobs & Durbin 2001). Care has been taken to avoid $\gamma = 0$, which does not correspond to any physical eigenvalue. The numerical method used to compute the eigenfunction of the homogeneous Orr–Sommerfeld and Squire operators follows the procedure described in Jacobs & Durbin (1998) and has been employed in Brandt *et al.* (2002). Thus, for a given wave-vector both an Orr–Sommerfeld and Squire mode are calculated and

the corresponding velocity components derived. An arbitrary phase shift is applied to both solutions before adding them into a velocity vector $\hat{\mathbf{u}}_N(y)$ normalized to unit energy. Note that since the individual eigenfunctions comply with continuity, their summation provides a disturbance which satisfies continuity as well. However, a numerical problem arises at the top of the computational domain. The high levels of free-stream perturbation at the top boundary limits the time step and can lead to numerical instabilities. Therefore the inflow perturbation is damped above a certain distance y_{dm} by multiplying the eigenfunctions with a smooth step function S . The following form for S , which has the advantage of having continuous derivatives of all orders, is used

$$S(y^*) = \begin{cases} 0, & y^* \leq 0 \\ 1 / \left[1 + \exp \left(\frac{1}{y^* - 1} + \frac{1}{y^*} \right) \right], & 0 < y^* < 1 \\ 1, & y^* \geq 1, \end{cases} \quad (2.4)$$

where

$$y^* = 1 - \frac{y - y_{dm}}{y_{max} - y_{dm}},$$

and y_{max} indicates the coordinate of the top boundary. The distance $y_{max} - y_{dm}$ is chosen to be $20\delta_0^*$, where δ_0^* is the boundary-layer thickness at the inflow of the computational domain.

The coefficients A_N used in the sum (2.3) provide a random phase, but the amplitude is defined so as to approximate a typical homogeneous- and isotropic-turbulence spectrum. In particular, the von Kármán spectrum is used

$$E(\kappa) \propto \frac{\kappa^4}{(C + \kappa^2)^{17/6}}. \quad (2.5)$$

Such a spectrum is for large scales asymptotically proportional to κ^4 , whereas it matches the Kolmogorov-(5/3)-low for small scales. Following the construction of a three-dimensional spectrum in Tennekes & Lumley (1972), an integral length scale L of the turbulence is introduced according to

$$L = \frac{1.8}{\kappa_{max}},$$

where κ_{max} is the wavenumber of maximum energy. Denoting by q the total turbulent kinetic energy, the following expression for the energy spectrum can be derived from (2.5)

$$E(\kappa) = \frac{2}{3} \frac{a(\kappa L)^4}{(b + (\kappa L)^2)^{17/6}} L q, \quad (2.6)$$

where $a = 1.606$ and $b = 1.350$. The length scale L_{11} defined from the longitudinal two-point correlation is related to L according to

$$L_{11} = \int_0^\infty \frac{\overline{u(x)u(x+r)}}{u^2} dr = \frac{3\pi}{4q} \int_0^\infty \frac{E(\kappa)}{\kappa} d\kappa \approx 0.643 L. \quad (2.7)$$

The energy is equally distributed among all modes on the same shell and therefore the coefficient of each of the terms in (2.3) is given by

$$A_N^2(\kappa) = E(\kappa) \frac{\Delta\kappa}{n_i},$$

	$x_1 \times y_1 \times z_1$ δ_0^*	$n_x \times n_y \times n_z$ (resolution)	$Re_{\delta_0^*}$
Box1	1000 \times 100 \times 90	1152 \times 201 \times 192	300
Box2	1000 \times 60 \times 50	1024 \times 121 \times 72	300
Box3	1000 \times 60 \times 50	1024 \times 121 \times 128	300
Box4	450 \times 100 \times 90	512 \times 201 \times 160	300

TABLE 1. Resolution and box dimensions for the simulations presented. The box dimensions includes the fringe region and are made dimensionless with respect to δ_0^* , the displacement thickness at the beginning of the computational box. The length of the fringe region is 90 for all cases under consideration. The total number of Fourier modes is indicated, corresponding to $n_x/2$ or $n_z/2$ conjugate pairs.

	Free-stream turbulence intensity (%)	Integral length scale l/δ_0^*	Computational domain
Case1	4.7	5	Box1
Case2	4.7	2.5	Box1
Case3	4.7	7.5	Box1
Case4	4.7	5	Box2
Case5	4.7	5	Box3
Case6	3	7.5	Box4
Case7	1.5	7.5	Box4
Case3 α	4.7	7.5	Box4
Case6 α	3	7.5	Box4
Case7 α	1.5	7.5	Box4

TABLE 2. Parameters used to define the free-stream turbulence and the corresponding computational domain for the cases presented. In all cases under consideration, 800 modes of the continuous spectrum of the Orr–Sommerfeld and Squire operators are employed. For the cases denoted by α , the free-stream turbulence generation is manipulated in order to involve many modes with very low values of the streamwise wavenumber α .

where $E(\kappa)$ is given in (2.6), $\Delta\kappa$ is the difference in wavenumber between two contiguous shells and n_i is the number of modes on each shell. For the simulations presented here, $\kappa_l = 0.23$, $\kappa_u = 3$ and $\Delta\kappa_l = 0.146$. For further details on the free-stream turbulence generation see Schlatter (2001).

2.3. Parameter settings

The box sizes and resolutions used for the simulations presented in this paper are displayed in table 1. The dimensions are reported in units of δ_0^* which denotes the Blasius boundary-layer displacement thickness at the beginning of the computational box which is set to $Re_{\delta_0^*} = 300$ for all cases under consideration. (Note that we will denote by δ^* the local displacement thickness as computed from its definition.) In all simulations performed, the length of the fringe region is chosen to be 90. The parameters used to define the free-stream turbulence and the corresponding computational domain for the cases presented are reported in table 2. In all cases under consideration, 800 modes of the continuous spectrum of the Orr–Sommerfeld and Squire operators are employed.

Box1 is used for the averaged results in §3.1 in which the effect of the free-stream turbulence length scales is also analysed. The analysis of the generation of the turbulent spots is performed with the results from the simulations with Box1 and,

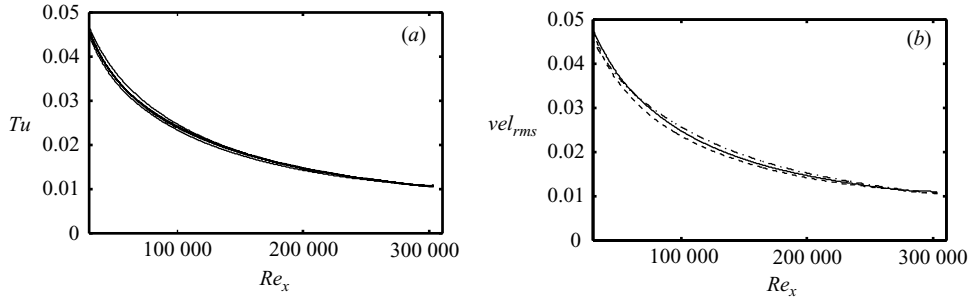


FIGURE 1. (a) Turbulence intensity versus the Reynolds number at 5 different heights above the boundary layer ($y/\delta_0^* = 30, 40, 50, 60, 70$; $L = 5\delta_0^*$). (b) Root mean square values of the three velocity components versus the Reynolds number for $L = 5\delta_0^*$ and $y/\delta_0^* = 40$. —, u_{rms} ; ---, v_{rms} ; ···, w_{rms} .

for the most of them, with the smaller Box2. The simulation labelled as Case5, using Box3, is used to check the resolution of the structures observed at the breakdown stage obtained with Box2. This proved to be more than satisfactorily. Box4 is employed for the simulations presented in §3.2. The focus of the section is on the initial phase of the transition process, i.e. the boundary-layer receptivity to free-stream turbulence and the streak growth, therefore a shorter computational domain is sufficient. For the cases denoted by α , the free-stream turbulence generation is manipulated in order to involve many modes with very low values of the streamwise wavenumber α , as described later.

3. Results

3.1. Averaged results: effect of the integral length scale of the incoming turbulence

The statistics obtained by averaging the velocity field in time and in the spanwise direction are presented in this section. Three cases, corresponding to Case1, Case2 and Case3 in table 2, are considered. For all of them, the free-stream turbulence intensity is 4.7%, whereas different integral length scales of the inflow turbulence have been used, that is $L = 2.5\delta_0^*$, $L = 5\delta_0^*$ and $L = 7.5\delta_0^*$. We show that the present simulations qualitatively reproduce the main features of the transition scenario observed in the experiments of a flat-plate boundary layer subject to upstream grid-generated free-stream turbulence and focus on how the response of the boundary layer varies with the length scales of the incoming turbulence.

3.1.1. Free-stream turbulence

We begin by documenting the free-stream turbulence induced by the methodology presented in the previous section. The objective of the implemented strategy was to force nearly isotropic and homogeneous turbulence in the free stream. In figure 1(a), the turbulence intensity $Tu = \sqrt{(u_{rms}^2 + v_{rms}^2 + w_{rms}^2)}/3$ is displayed versus the Reynolds number based on the distance from the leading edge $Re_x = xU_\infty/\nu$, at 5 positions above the boundary layer to show the degree of homogeneity achieved. The difference in the level of the fluctuations among the velocity components for one selected wall-normal distance is shown in figure 1(b).

A comparison of the features of the artificial free-stream turbulence in the three cases under consideration is displayed in figure 2 by the downstream decay of the turbulence intensity at a position far above the boundary layer. The data in the

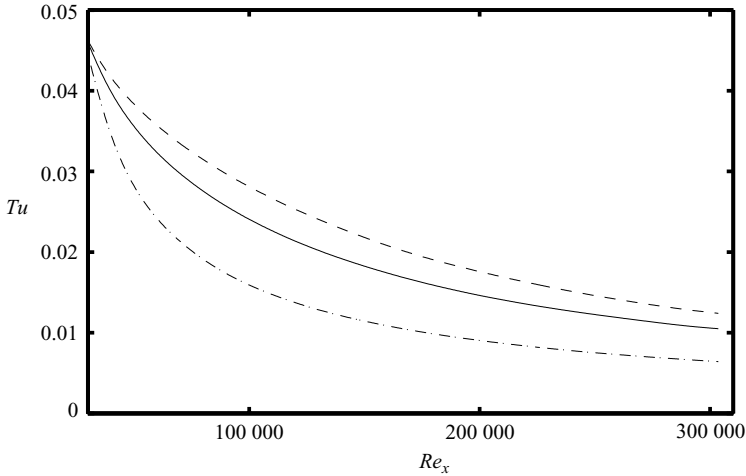


FIGURE 2. Turbulence intensity decay for the free-stream turbulence length scales considered: ---, $L = 7.5\delta_0^*$; —, $L = 5\delta_0^*$; - · -, $L = 2.5\delta_0^*$.

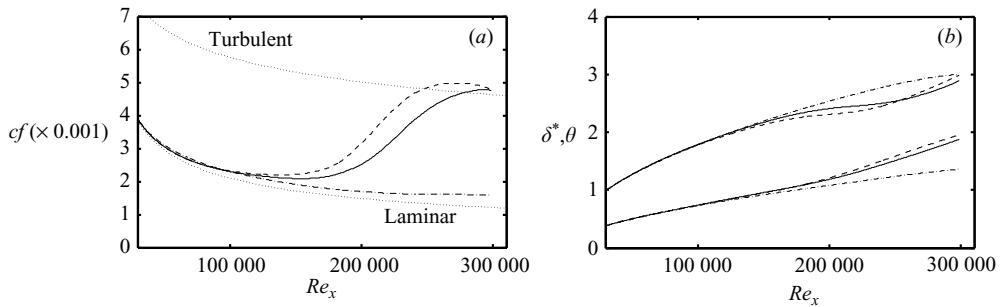


FIGURE 3. (a) Skin friction coefficient and (b) boundary-layer displacement and momentum-loss thickness for the free-stream turbulence length scales considered: ---, $L = 7.5\delta_0^*$; —, $L = 5\delta_0^*$; - · -, $L = 2.5\delta_0^*$.

figure have been analysed and it is possible to show that the decay obeys a power law in agreement with experimental works on isotropic homogeneous turbulence. As expected, the turbulence decay decreases for increasing length scales.

3.1.2. Effect of the integral length scale on the boundary-layer transition

The skin friction coefficient provides a good indication of the transition location. This is shown for the three cases considered in figure 3(a); also, the values for a laminar and a turbulent boundary layer are displayed for comparison. For the case with the smallest integral length scale, transition does not occur within the computational domain, while for the largest values of L , a turbulent flow is observed at the end of the domain. The completion of the transition is at lower Re_x for $L = 7.5\delta_0^*$, thus confirming the trend observed in the experimental study of Jonáš, Mazur & Uruba (2000). The transition location in the present simulations is only slightly upstream of that observed in the experiments by Matsubara *et al.* (2000) and Roach & Brierley (1990) (test case T3A) with a lower free-stream turbulence level of 3%. However, the difference is not so surprising: in the experiments the turbulence affects the boundary layer from the leading edge, while in the simulations it is induced a certain distance

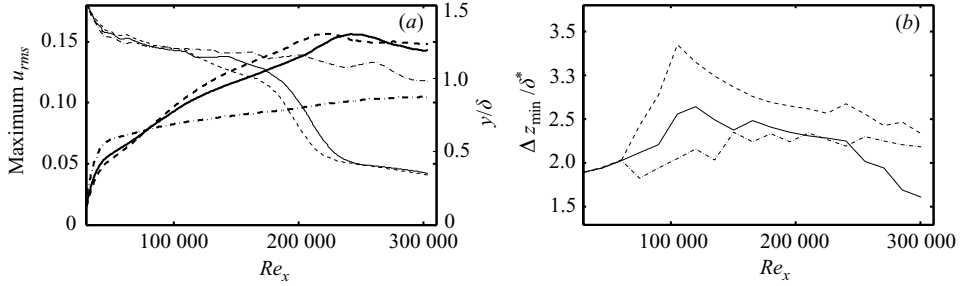


FIGURE 4. (a) maximum u_{rms} (thick lines) and its wall-normal position (thin lines), and (b) first minimum of R_{13} scaled with the local displacement thickness δ^* for the integral length scales: - - -, $L = 7.5\delta_0^*$; —, $L = 5\delta_0^*$; - · -, $L = 2.5\delta_0^*$.

downstream. Moreover, the inlet perturbation used for the simulations in the figure has low energy content in its low-frequency components and, as will be discussed in §3.2, this has a strong influence on the receptivity phase and, as a consequence, on the streak amplitudes. Note also that the lower decay of the free-stream turbulence in the case of Roach & Brierley (1990) lead us to believe that a larger integral length scale characterizes the grid-generated turbulence.

Figure 3(b) shows the development of the boundary-layer displacement and momentum-loss thicknesses δ^* and θ . The development for a laminar Blasius boundary layer is very close to that for $L = 2.5\delta_0^*$, when transition is not observed. In close agreement to the experimental findings of Matsubara & Alfredsson (2001), the displacement thickness is seen to decrease slightly below the laminar values in the transitional region (cf. figure 3a), and then to increase faster in the quasi-turbulent flow. The momentum loss is always larger than in the laminar case because the skin friction increases owing to the occurrence of the turbulent spots. A similar peculiar decrease of the boundary-layer displacement thickness is observed in the numerical simulations of the breakdown of a single steady streak subject to sinuous instability by Brandt & Henningson (2002).

Perturbations enter the boundary layer in the form of low-frequency fluctuations, mainly in the streamwise velocity component, i.e. of streamwise streaks. The maximum u_{rms} at each downstream position is displayed in figure 4(a). The perturbation is initially largest in the case of $L = 2.5\delta_0^*$, indicating that the smallest scales penetrate more easily into the boundary layer. However, this growth cannot be sustained further downstream as in the other cases. A plausible explanation is that the free-stream turbulence decays faster for smaller L and therefore it is less effective in continuously forcing the streaks along the plate. The necessity of a continuous forcing on the streaks from the free stream was pointed out in Westin *et al.* (1998). Note also that it was shown in Brandt *et al.* (2002) that the large scales induce stronger streaks in the boundary layer, but on a longer time. In figure 4(a), the wall normal position of maximum u_{rms} is also shown. The laminar streaks have a maximum at about $y = 1.3\delta^*$ in agreement with the experimental data in Matsubara & Alfredsson (2001), while their turbulent counterparts, at the end of the domain, are located closer to the wall.

In figure 4(b), we display the evolution of the first minimum of the spanwise correlation of the streamwise velocity fluctuations at the wall-normal position of maximum u_{rms} ; this is a measure of half the spanwise wavelength of the streaks. It can be seen from the figure that the length scale of the perturbation inside the boundary layer is only slightly dependent on the free-stream turbulence characteristic

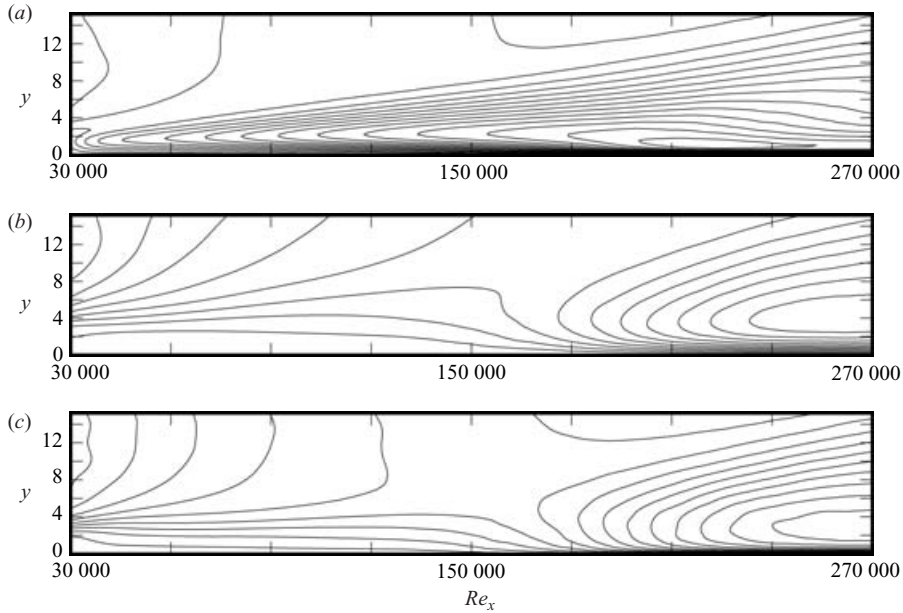


FIGURE 5. Wall-normal distribution of the r.m.s. values of the three velocity components versus the streamwise position for the simulation with $L = 7.5\delta_0^*$. (a) Streamwise component; (b) wall-normal component; (c) spanwise component. The wall-normal coordinate is scaled by the inflow displacement thickness δ_0^* . Contour levels: u min 0.01, max 0.15, spacing 0.01; v min 0.005, max 0.05, spacing 0.005; w min 0.005, max 0.065, spacing 0.005.

scale. The spanwise scales observed are in agreement with the experimental results of Matsubara & Alfredsson (2001); the values obtained are slightly lower than those pertaining to the linear optimal perturbation computed by Andersson *et al.* (1999) and Luchini (2000).

Note also that in the cases in which transition does occur, the streak spacing decreases downstream once scaled with the local displacement thickness, indicating that the streak physical wavelength stays almost constant. On the contrary, in the case with smallest integral length scale L , the streak spacing stays constant once scaled with the local displacement thickness, indicating that the streak wavelength increases downstream.

The wall-normal distribution of the r.m.s. values of the three velocity components is displayed versus the streamwise position in figure 5 for the simulation with $L = 7.5\delta_0^*$. The cross-stream velocity fluctuations are weak compared to the u_{rms} and a distinct peak inside the boundary layer can be seen only at the streamwise positions where turbulent spots are observed and the streaks are of a more turbulent nature.

A comparison between the wall-normal profile of the linear optimal streak computed by Andersson *et al.* (1999) and u_{rms} profiles extracted in the pretransitional region of the present simulations is shown in figure 6. A similarly remarkable agreement between theory and experimental data is also found in Andersson *et al.* (2001) and Matsubara & Alfredsson (2001). Luchini (2000) noted that the shape of the streak always tends to be attracted towards the shape of the optimal perturbation, even for a generic initial perturbation (provided not orthogonal to the optimal). The universal profile that the streak tends to assume is very close to a simple thickness modulation, just as empirically observed by Taylor (1939). (A discussion of the

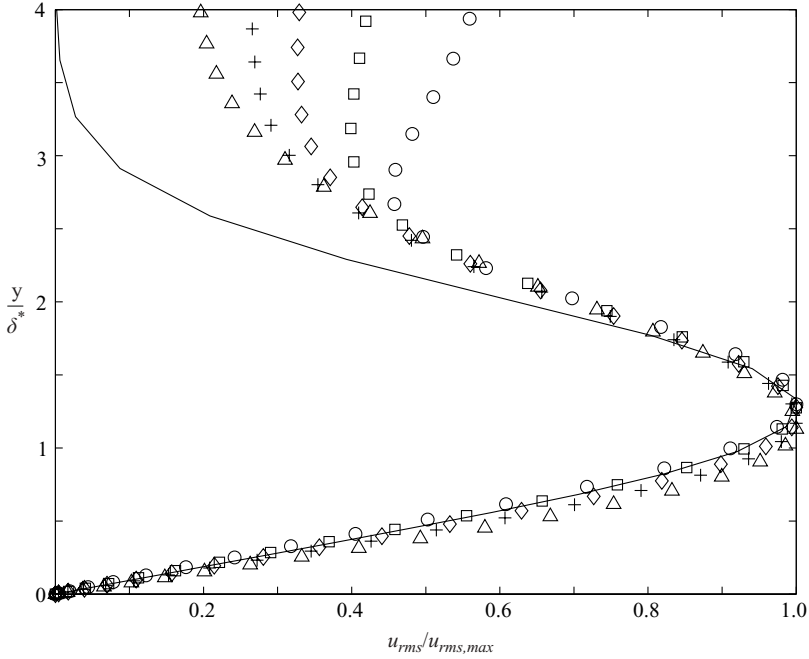


FIGURE 6. Comparison between the wall-normal profile of the streamwise velocity component of the downstream response to the optimal perturbation in Andersson *et al.* (1999), depicted with the solid line, and the u_{rms} data from the simulation Case1. The symbols represent profiles extracted at: \circ , $Re_x = 4.5 \times 10^4$ ($u_{rms,max} = 0.054$); \square , $Re_x = 6 \times 10^4$ ($u_{rms,max} = 0.064$); \diamond , $Re_x = 7.5 \times 10^4$ ($u_{rms,max} = 0.074$); $+$, $Re_x = 9 \times 10^4$ ($u_{rms,max} = 0.086$); \triangle , $Re_x = 1.2 \times 10^5$ ($u_{rms,max} = 0.097$).

relation between optimal perturbation and displacement analysis can be found in Luchini 2001.) The streak can therefore be considered as a pseudo-mode triggered in boundary layers subject to significant outside disturbances.

Before discussing in detail the instantaneous flow configurations, a new quantity is introduced to try to follow better the development of the perturbation in the laminar boundary layer. The amplitude of the streak is not averaged in time, but the maximum and minimum of the local streamwise disturbance velocity during the integration time is stored. Formally, the quantities $\hat{u}_{max}(x, y)$ and $\hat{u}_{min}(x, y)$ are defined by

$$\hat{u}_{max}(x, y) = \max_{t,z}[u(x, y, z, t) - \bar{u}(x, y, t)],$$

$$\hat{u}_{min}(x, y) = \min_{t,z}[u(x, y, z, t) - \bar{u}(x, y, t)],$$

where $\bar{u}(x, y, t)$ denotes the spanwise average of the instantaneous velocity $u(x, y, z, t)$. The downstream evolution of the wall-normal maximum of $\hat{u}_{max}(x, y)$ and $\hat{u}_{min}(x, y)$ is displayed in figure 7. It can be seen that the value of the maximum perturbation is not so different among the three cases considered. The highly irregular oscillations, indicating the appearance of a turbulent spot, are clearly visible at the end of the displayed domain. These oscillations continue downstream for all the cases considered. Note also that these strong oscillations are first seen in \hat{u}_{min} , confirming the fact that the breakdown is initiated on the low-speed regions. Figure 7 enables us to explain better the differences observed in the time-averaged results (cf. figures 3a and 4a). In the case of the smallest integral length scale, strong streaks and turbulent spots also

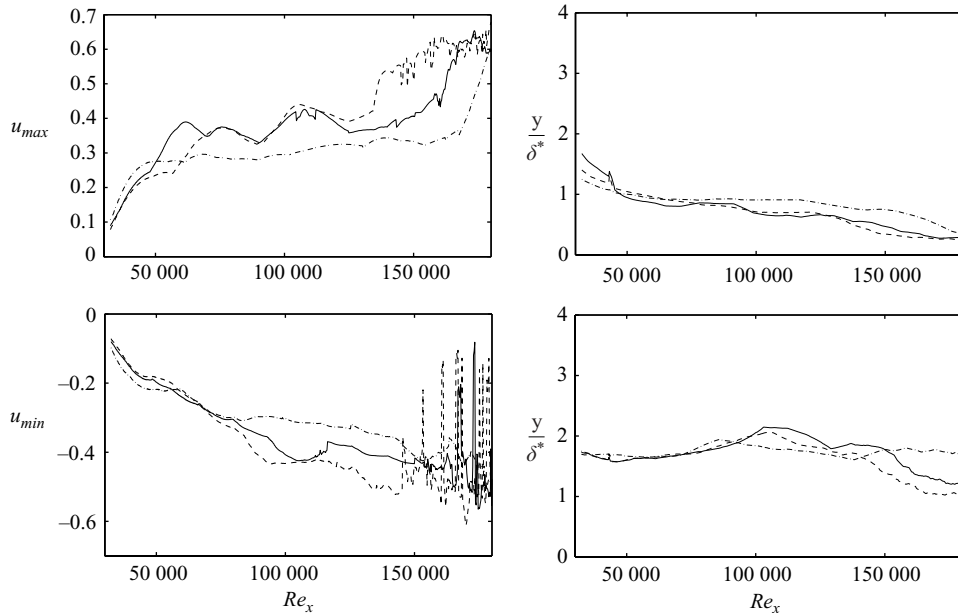


FIGURE 7. Streamwise evolution of the maximum of the streamwise velocity perturbation \hat{u}_{max} (see definition in the text) and its wall-normal position (top two figures). Minimum of u_{min} and its wall-normal position (bottom two figures). Plotted for the integral length scales: ---, $L = 7.5\delta_0^*$; —, $L = 5\delta_0^*$; - · -, $L = 2.5\delta_0^*$.

occur in the boundary layer, however, the fact that the time-averaged quantities are hardly affected indicates that it happens seldom. The difference appears, hence, to be related to the number and frequency of occurrence of the single events. In agreement with the r.m.s. values in figure 4(a), the growth of the perturbations decreases earlier ($Re_x \approx 80\,000$) in the simulation with the free-stream turbulence length scale $L = 2.5\delta_0^*$.

The values of the streak amplitudes are much larger than the corresponding r.m.s. The fact that the averaged values usually reported in the experiments are likely to mask stronger localized distortions, which are able to induce the breakdown, was first suggested by Wundrow & Goldstein (2001). The streaks soon reach an amplitude of the order of 30% of the free-stream velocity, a sufficiently high value for the onset of a secondary instability (Andersson *et al.* 2001). The maximum positive and negative streamwise velocity perturbations exhibit a different wall-normal distribution. This can be seen in figure 7 where the y -position of the peak of the high- and low-speed streaks is also displayed. The high-speed streak is, in fact, located closer to the wall while the low-speed streak is pushed in the upper part of the boundary layer by the lift-up effect. A spatial perspective view of the lift-up effect and streak location can be found in Jacobs & Durbin (2001) (cf. figure 16).

3.2. Streamwise streak receptivity

3.2.1. Background: proposed receptivity mechanisms

In this section, we look in detail at the initial phase of the transition process, i.e. the boundary-layer receptivity to free-stream turbulence and the streak formation and following growth. The results presented refer to Case3, Case6, Case7 and Case3 α , Case6 α , Case7 α in table 2, for which a shorter computational domain is used. In the literature, two possible mechanisms for the streak generation in boundary layers

subject to free-stream turbulence have been proposed: a linear and a nonlinear one. A linear mechanism for streak generation caused by the diffusion and/or propagation of a free-stream streamwise vortex into the boundary layer has been studied by Andersson *et al.* (1999) and Luchini (2000) using the boundary-layer equations and by Wundrow & Goldstein (2001) by means of asymptotic expansions. These studies assume the presence of streamwise vorticity at the leading edge. Bertolotti (1997) and Bertolotti & Kendall (1997) focused on the continuous forcing from free-stream low-frequency vortices, but still studied a linear mechanism. If a linear receptivity model is considered, the growth of the streaks is directly induced by the streamwise vortices and it turns out to be proportional to the Reynolds number $Re_\delta \sim \sqrt{Re_x}$. In Berlin & Henningson (1999) and Brandt *et al.* (2002) a nonlinear model for receptivity, originating from the interactions of oblique modes in the free stream, has been proposed. This mechanism can be reduced to a two-step process, first the nonlinear generation of streamwise vorticity penetrating the boundary layer due to nonlinear interactions and then the formation of streaks due to the linear ‘lift-up’ effect. For this nonlinear scenario, it has been found that the streak amplitude is proportional to an amplification factor of the order $O(Re_\delta^2)$ times the square of the amplitude of the outside perturbation. In contrast, the linear model assumes a stronger direct forcing proportional to the amplitude of the perturbation, but it requires the presence of streamwise vorticity inside the boundary layer.

Here, by means of DNS, we would like to compare the two mechanisms and try to identify which of the two can be considered as the most relevant in cases with known free-stream perturbation. In order to do so, different levels of free-stream turbulence intensity are considered and, for the cases denoted by α , the free-stream turbulence generation is manipulated in order to involve many modes with very low values of the frequency ω and, consequently, of the streamwise wavenumber α . This is achieved by constraining the rotation of the dodecahedra used to determine the wavenumber of the modes in the inflow disturbance expansion described in §2.2. For the completely random inflow used in Case3, Case6 and Case7, only 4.5% of the modes have a wavenumber $\alpha < 0.05$. By allowing a fully random rotation of the dodecahedra only around the ω -axis, which is achieved by multiplying the rotation angles with respect to the β and γ directions by 0.0015, the percentage of low-frequency modes ($\alpha < 0.03$) in the expansion is increased to 20%. Note that this change leaves the energy spectrum of the free-stream turbulence the same as a function of the absolute value of the three-dimensional wave-vector κ . As shown by Hultgren & Gustavsson (1981) among others, modes of the continuous spectra with very low α and ω values do not feel the shear layer and they are therefore not zero inside the boundary layer. This property of the continuous spectrum modes reflects the fact that high-frequency perturbations are damped inside the boundary layer by inviscid shearing (Craik 1991), while low-frequency perturbations can diffuse into the boundary layer. It is shown in Jacobs & Durbin (1998) that the penetration depth of the continuous modes inside the shear layer is inversely proportional to the Reynolds number. Note, finally, that the results of this receptivity study are obtained for a fixed value of the integral length scale, $L = 7.5\delta_0^*$.

3.2.2. Results and discussion

High-frequency free-stream perturbations and nonlinear receptivity

First, the results obtained when the artificial inflow turbulence is mainly associated with high-frequency disturbances are discussed; these are Case3, Case6 and Case7 in

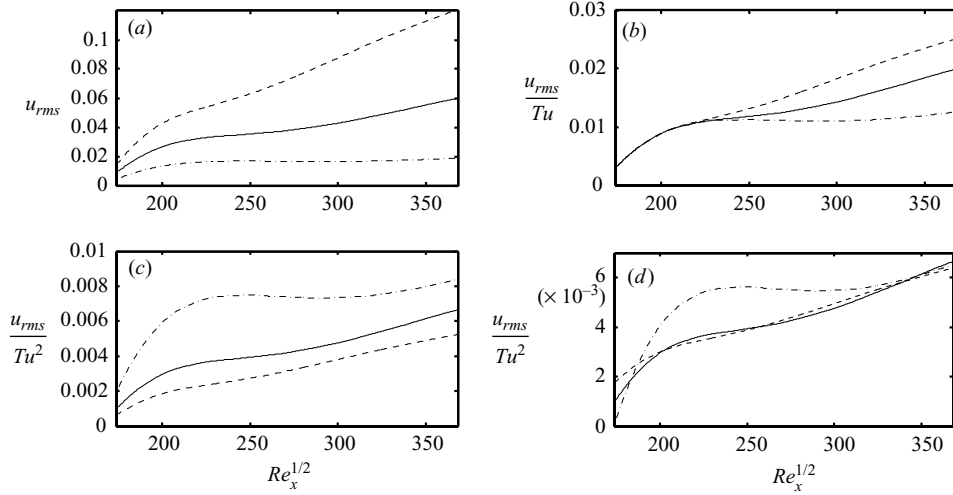


FIGURE 8. (a) Streamwise evolution of the wall-normal maximum of u_{rms} for the simulations with: ---, $Tu = 4.7\%$; —, $Tu = 3\%$ - · - ·; $Tu = 1.5\%$. The same r.m.s.-values are scaled with the inlet free-stream turbulence intensity Tu and Tu^2 in (b) and (c), respectively. In (d), the values divided by Tu^2 are translated in order to account for the different initial phases of the development.

table 2. The downstream evolution of the wall-normal maximum of the streamwise velocity perturbation is reported in figure 8. The square root of the Reynolds number $Re_x^{1/2}$ is used as streamwise coordinate in this section. This is chosen because linear optimal-growth theory predicts that the amplification of the streak energy is proportional to Re_x or equivalently

$$u_{rms} \sim Re_x^{1/2} Tu, \quad (3.1)$$

where Tu indicates the turbulence intensity at the inlet. In figure 8(a), the amplitude attained by the streaks is shown for the three different free-stream turbulence intensities Tu under consideration. Note that the perturbation level remains low for the weakest amplitude of the inflow perturbation. The same r.m.s. values are divided by Tu in figure 8(b) and by Tu^2 in figure 8(c). From figure 8(b), it can be seen that the initial growth of the perturbation inside the boundary layer scales linearly with Tu . At this early stage, the growth is most probably associated with the initial adjustment of the artificial inlet turbulence. It can be seen in figure 4 that these initial perturbations also have different wall-normal maximum and spanwise scales when compared to the features of the high-amplitude streaks emerging in the transitional region (note that $Re_x^{1/2} < 225$ corresponds to $Re_x < 50\,000$). After this initial phase, the growth is faster for larger Tu and it can be seen in figure 8(c) that the streak amplitude follows almost parallel lines when the u_{rms} is scaled with the square of the free-stream turbulence intensity. This is more evident for the two largest values of Tu . To more clearly show, that the growth of the streaks scales with Tu^2 and hence is governed by the nonlinear mechanism, the curves in figure 8(c) are translated in order to compensate for the different initial part of the development and displayed in figure 8(d). The dashed curve, pertaining to the case with $Tu = 4.7\%$, has been vertically translated to have the same value as the solid line, pertaining to the case with $Tu = 3\%$, at $Re_x^{1/2} = 205$, where the two corresponding curves begin to diverge in figure 8(b). The dash-dotted curve, Case7 with $Tu = 1.5\%$, has been

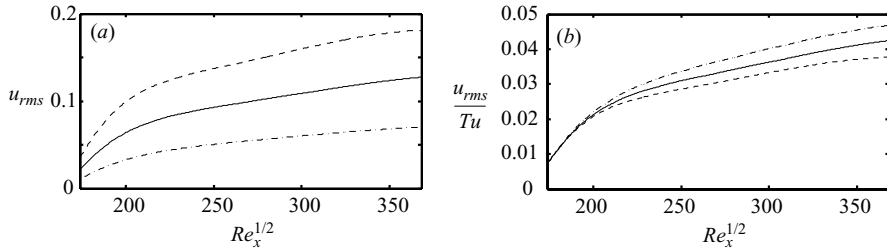


FIGURE 9. (a) Streamwise evolution of the wall-normal maximum of u_{rms} for the simulations with low-frequency modes as part of the inflow perturbation spectrum (Case3 α , Case6 α and Case7 α) and for: ---, $Tu = 4.7\%$; —, $Tu = 3\%$; - · -, $Tu = 1.5\%$. (b) The same r.m.s.-values are scaled with the free-stream turbulence intensity Tu .

moved downwards to coincide with the solid line at $Re_x^{1/2} = 340$. For this case, the growth of the streak seems to scale quadratically only from this downstream station. The amplitude of the nonlinear interactions, $O(Tu^2)$, is much weaker in this case and their effect is felt further downstream. Note that no growth is observed in the region between $Re_x^{1/2} = 235$ and $Re_x^{1/2} = 340$, where the global energy associated to the low-frequency modes of the inflow spectrum has ceased to grow.

Thus, after an initial phase in which the growth of the perturbation in the boundary layer is linear and involves the low-frequency disturbances already part of the inflow turbulence, the nonlinear mechanism discussed above takes over and becomes dominating. A certain distance (and time) is required for the nonlinear process to take place; however, this distance can be regarded as small. Note that this nonlinear receptivity process is also observed in the simulations by Jacobs & Durbin (2001). These authors show that the inflow perturbation spectrum evolves downstream into a different perturbation spectrum through the generation and successive amplification of the low-frequency components. Also in agreement with the data in Jacobs & Durbin (2001), the streamwise growth of the streaks is found to be proportional to $Re_x^{1/2}$. Therefore, if the nonlinear mechanism is clearly dominating, the following expression can be suggested to describe the perturbation behaviour

$$u_{rms} \sim Re_x^{1/2} Tu^2. \quad (3.2)$$

Low-frequency free-stream perturbations and linear receptivity

The results obtained for the corresponding cases denoted by α are reported in figure 9. Owing to the manipulation of the modes yielding the inflow perturbation, larger values of u_{rms} are now attained inside the boundary layer already at the inlet ($Re_x^{1/2} = 175$), where the perturbation consists of the low-frequency modes of the continuous spectra. For the case with $Tu = 4.7\%$, turbulent spots are observed during the integration time already within the shorter computational box used for this type of simulation. The transition location would then be moved upstream as compared to the simulation Case3 in figure 3. The sensitivity of the transition location not only to the free-stream turbulence length scales but also to its spectral content, as shown here, can further account for the difference among the numerical simulations and experimental results (Roach & Brierley 1990; Matsubara *et al.* 2000), as well as among experiments performed with different set-ups (Westin *et al.* 1994).

A fairly good collapse of the three u_{rms} curves in figure 9(a) is obtained if their values are divided by the free-stream turbulence intensity as in figure 9(b). The streak

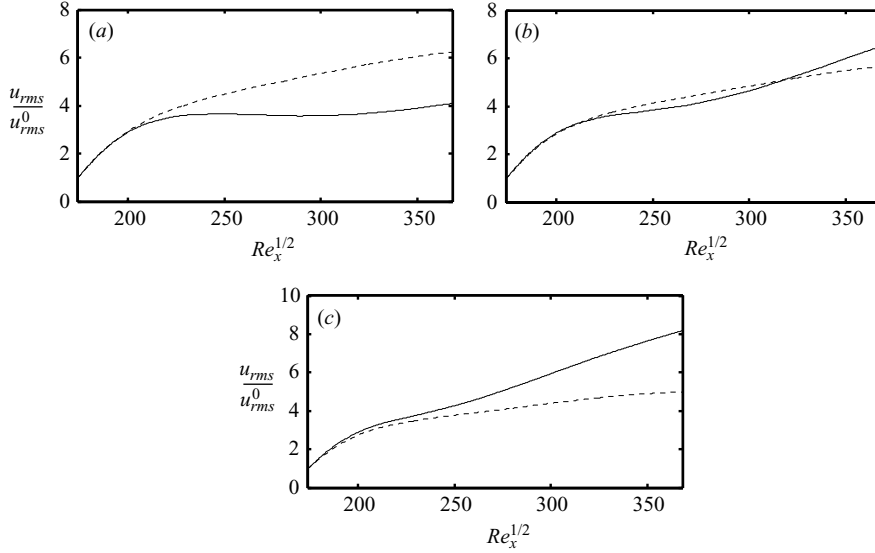


FIGURE 10. Streamwise evolution of the wall-normal maximum of u_{rms} normalized by its value at the inlet u_{rms}^0 for: (a) the simulations denoted by Case7 ($u_{rms}^0 = 0.46\%$) and Case7 α ($u_{rms}^0 = 1.13\%$), with $Tu = 1.5\%$; (b) the simulations denoted by Case6 ($u_{rms}^0 = 0.92\%$) and Case6 α ($u_{rms}^0 = 2.25\%$), with $Tu = 3\%$; (c) the simulations denoted by Case3 ($u_{rms}^0 = 1.48\%$) and Case3 α ($u_{rms}^0 = 3.64\%$), with $Tu = 4.7\%$. The dashed lines indicate the cases denoted by an α .

growth is slightly decreasing for increasing levels of Tu , as shown by the opposite order of the three curves when compared with the results in figure 8(b), which can be explained by the saturation occurring for the large u_{rms} observed. Thus, if significant low-frequency perturbations can impinge directly on the boundary layer, the linear mechanism becomes the dominating process responsible for the streak formation and growth.

Linear versus nonlinear receptivity

We would now like to compare the streak amplification occurring when the two different receptivity mechanisms are at work while keeping the level of free-stream turbulence constant. In order to do so, the downstream evolution of the wall-normal maximum of u_{rms} inside the boundary layer is normalized by the perturbation intensity at the inlet u_{rms}^0 , defined as the maximum value inside the boundary layer. The latter is an indirect measure of the low-frequency energy content of the free-stream turbulence since only modes of the continuous spectrum with low ω are non-zero inside the boundary layer. The ratio $(u_{rms}^0/Tu)^2$ is therefore proportional to the fraction of free-stream turbulence energy in low-frequency modes. The u_{rms} -values downstream indicate the level of low-frequency perturbation growing inside the boundary layer. If the linear receptivity process is active, the r.m.s.-values reflect the amplification of the low-frequency part of the free-stream turbulence spectrum. If, conversely, the nonlinear process is dominant, low-frequency perturbations are induced by quadratic interactions among high-frequency modes. The normalized data are plotted in figure 10 for the three different levels of free-stream turbulence and the two different levels of relative energy content in low-frequency modes. For the lowest $Tu = 1.5\%$ in figure 10(a), the streak growth is larger for the case with relatively

high levels of energy in low-frequency modes, in which case the relevant receptivity mechanism is linear. However, for a free-stream turbulence intensity of 3%, the total amplification of the streamwise velocity perturbation inside the boundary layer is of the same order, independently of the relative level of low-frequency content and of which of the two mechanisms is dominating (see figure 10*b*). In figure 10*c*), the comparison for the two simulations with $Tu = 4.7\%$ is displayed. The amplification is larger when the nonlinear receptivity mechanism is dominating, in spite of the fact that the actual r.m.s. values are larger for Case3 α . Thus, we can conclude that the largest amplification of the streamwise velocity perturbation inside the boundary layer is obtained with the linear mechanism for low levels of free-stream turbulence, while the nonlinear streak induction process becomes stronger for larger values of the incoming perturbations, $Tu \gtrsim 3\%$.

Relation to transition prediction

In many of the referenced experimental studies (Roach & Brierley 1990; Westin *et al.* 1994; Matsubara & Alfredsson 2001), the u_{rms} is shown to be proportional to $Re_x^{1/2}$. The present simulations further confirm this finding and indicate that the slope m of the curve $u_{rms} \sim m Re_x^{1/2}$ is proportional to Tu if the linear receptivity mechanism is at work or to Tu^2 if the nonlinear receptivity is dominating. Based on optimal growth calculations for boundary-layer flow, a transition prediction model is suggested by Andersson *et al.* (1999). The proposed model exploits the relation (3.1) and assumes that transition is triggered when the u_{rms} value reaches a critical threshold. Combining the two assumptions, we find that the transition location Re_T is related to the free-stream turbulence intensity by

$$Re_T^{1/2} Tu = \text{const.}$$

If the nonlinear mechanism is the most relevant, we can alternatively use relation (3.2) and obtain

$$Re_T^{1/2} Tu^2 = \text{const.}$$

The prediction based on the linear receptivity is shown to apply well to free-stream turbulence levels lower than 6% (see the experimental data in Matsubara *et al.* 2000). More recently, Fransson (2003) and Fransson, Matsubara & Alfredsson (2004) showed that the u_{rms} growth is proportional both to Tu and to $Re_x^{1/2}$. Following the discussion above, we can conclude that the linear process is therefore the dominating receptivity mechanism in the considered experiments. This is most probably due to the fact that the turbulence is generated by a grid located upstream of the leading edge and the low-frequency perturbation components decay more slowly than those of higher frequency. For many of these experiments, the free-stream turbulence level is less than 3%, the value below which the amplification due to the linear mechanism is found to be largest (see figure 10). For higher values of Tu , the amount of low-frequency energy of the incoming perturbation is high enough to more than balance the greater amplification associated with the nonlinear receptivity mechanism.

3.3. Turbulent spot generation

In this section, we analyse the breakdown by looking at the instantaneous three-dimensional flow configurations for a number of spots, tracing back in time the location of their formation. A snapshot of the flow is shown in figure 11 where the instantaneous streamwise and spanwise velocities are plotted in a plane parallel to the wall. The overall picture of the transition scenario can be deduced from the

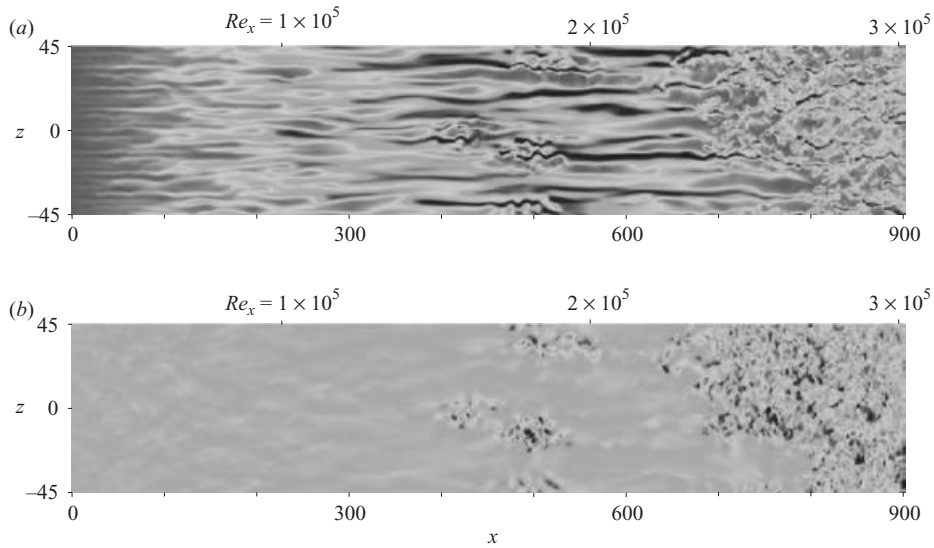


FIGURE 11. (a) Instantaneous streamwise velocity and (b) spanwise velocity in a plane parallel to the wall at $y/\delta_0^* = 2$ from simulation Case3. The plots are not at the actual scale since the domain depicted is 900 units long and 90 units wide in terms of δ_0^* . The fringe region is not shown.

figure. Starting from the inlet position, the perturbation in the boundary layer appears mainly in the streamwise velocity component, in the form of elongated structures. Patches of irregular motion are seen to appear further downstream; these are more evident in the spanwise component. For this reason, the cross-stream velocities will be used in the following to identify the perturbation riding on the streaks so that a ‘natural’ separation is obtained between the streaks and the growing high-frequency irregular motions observed. As they travel downstream, the spots become wider and longer. Note also that laminar streaks can be observed downstream of the spots. The turbulent region at the end of the domain is created by the enlargement and merging of the various spots and therefore the streamwise position at which the flow is turbulent varies with time; the turbulent flow is convected downstream and it would not be seen if new spots were not formed continuously.

To trace back in time the birth of a turbulent spot, (x, z) -planes at different wall-normal distances are saved during the numerical integration of the Navier–Stokes equations. Full three-dimensional velocity fields could then be saved at chosen times by repeating the same computation. An important feature of the spot precursors, observed in all cases considered, is the presence of regions of positive and negative wall-normal and spanwise velocity arranged in a quasi-periodic pattern. This region of disturbed flow is growing while travelling downstream in the typical manner of a wave packet. An example of this is shown in figures 12 and 15. The regular distribution of cross-stream velocities is responsible for the associated wavy motion of the streak preceding the breakdown. Visual inspection of many velocity fields shows that it is possible to classify the type of breakdown occurring on the streaks by considering the spanwise symmetry of the wall-normal and spanwise velocities and the location relative to the underlying streak.

The symmetry of the high-frequency perturbations initiating the breakdown and the structures characterizing the incipient spots resemble those observed in the studies on

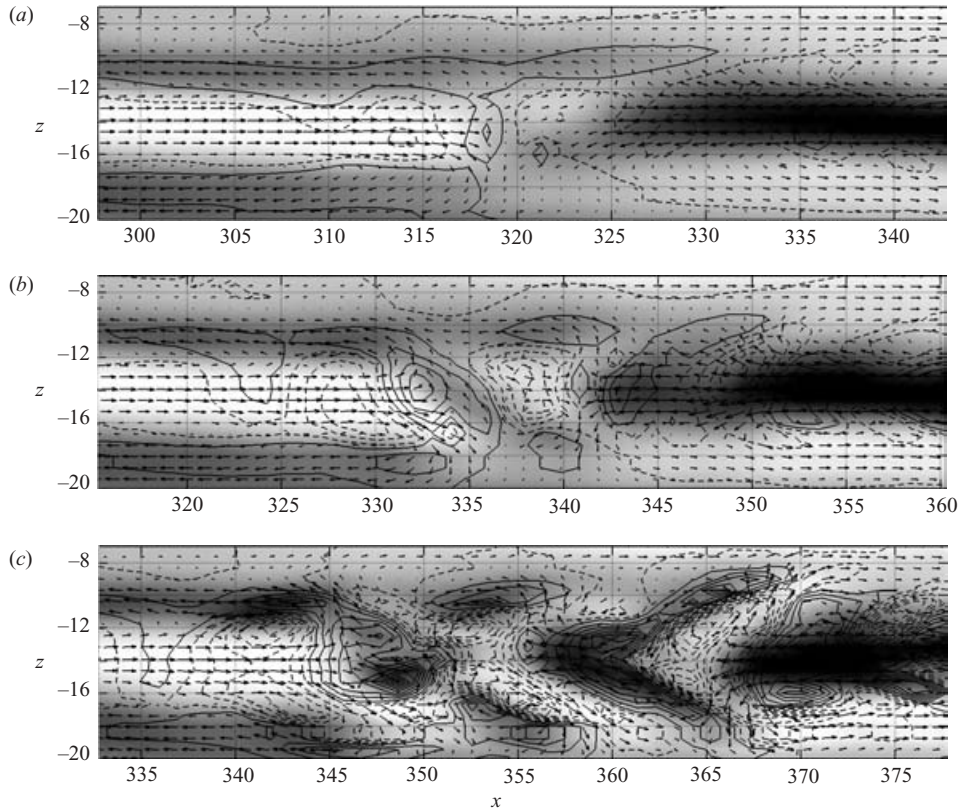


FIGURE 12. Time sequence showing the evolution of a typical varicose-like breakdown in a plane parallel to the wall ($y/\delta_0^* = 2.5$). The velocity vectors represent the streamwise perturbation velocity u' and the spanwise velocity w . Black lines represent isocontours of wall-normal velocity of value $\pm 0.0075, \pm 0.0225, \pm 0.0375 \dots$ (dashed lines indicate the negative values). The background shows values of streamwise velocity u' from negative values (dark areas) to positive (light areas). From top to bottom $t' = 0, 25, 50$. The displayed area moves at $c = 0.7U_\infty$ to maintain the perturbation in the picture. The range $x \in [297, 377]$ corresponds to $Re_x \in [1.19 \times 10^5, 1.43 \times 10^5]$ and the data are extracted from simulation Case4.

the breakdown of steady symmetric streaks, both in the sinuous case (Brandt & Henningson 2002) and in the varicose case (Asai *et al.* 2002). Therefore, we refer to them as sinuous-like and varicose-like breakdown. The former scenario is observed most frequently, with sinuous-like breakdown in 16 of the 28 spots considered. Note that here the secondary instability is not forced continuously, but triggered locally and therefore develops as a localized wave packet, as in the study of secondary instability wave packets recently performed by Brandt *et al.* (2003). Although the disturbances are neither completely symmetric nor antisymmetric as in the model problems mentioned above, the velocities show almost the same pattern with respect to the mean shear of the streaks. The case of the varicose-like breakdown is characterized by a symmetric distribution of the high-frequency components of u and v with respect to the middle of the low-speed region, while the spanwise velocity w assumes an antisymmetric pattern. In the varicose case, previous studies have shown that the wall-normal shear of the basic streamwise flow is driving the instability (e.g. Skote, Haritonidis & Henningson 2002). In the case of sinuous breakdown, the streaks

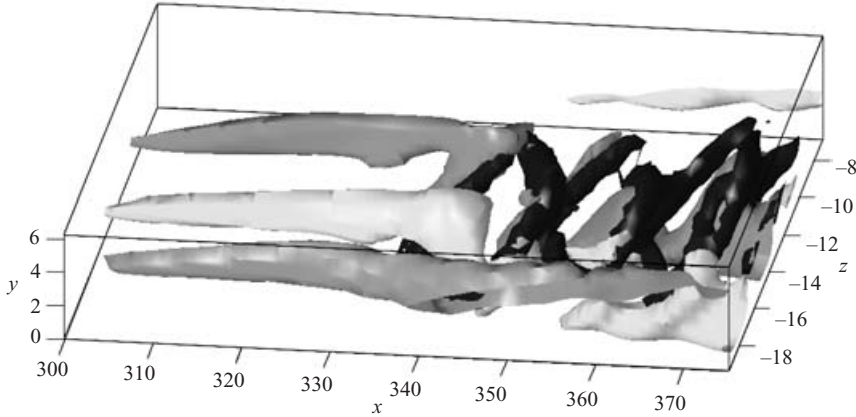


FIGURE 13. Instantaneous flow configuration at the varicose-like breakdown of a streamwise streak. Light grey represents positive perturbation streamwise velocity ($u' = 0.13$), while dark grey indicates the low-speed streak ($u' = -0.13$). The black structures are regions of negative λ_2 , used to identify vortical structures. The range $x \in [300, 375]$ corresponds to $Re_x \in [1.2 \times 10^5, 1.43 \times 10^5]$ and the data are extracted from simulation Case4 at time $t' = 49$ (see figure 12).

undergo spanwise antisymmetric oscillations and the perturbation kinetic energy production is driven by the spanwise shear of the streaky flow as first observed by Swearingen & Blackwelder (1987). In the sinuous-like scenario the streamwise and wall-normal perturbation velocities assume an antisymmetric distribution, while the spanwise component is symmetric with respect to the low-speed streak.

3.3.1. Varicose-like breakdown

The appearance of the varicose-like or symmetric breakdown has been shown to be governed by Kelvin–Helmholtz-like instability of inflectional wall-normal profiles and the transition scenario is characterized by the appearance of horse-shoe or Λ -structures. An example of the flow typically observed in the varicose-like scenario is depicted by the time sequence in figure 12. The figure follows the evolution of the growing wave-packet in the (x, z) -plane at $y/\delta_0^* = 2.5$ moving at speed $c = 0.7U_\infty$ in order to maintain the perturbation in the figure. The background colour shows the low- (dark areas) and high-speed streak (light areas), the contour levels depict the wall-normal velocity, while the velocity vectors represent the streamwise velocity u' , defined as the difference between the instantaneous streamwise velocity $u(x, y, z, t)$ and its spanwise average $\bar{u}(x, y, t)$, and the spanwise velocity w . It can be seen in the figure that the wave packet is induced between an oncoming high-speed streak and a downstream low-speed region and then develops mainly on the low-speed streak. The strong wall-normal velocity perturbation is centred on top of the streak with positive and negative values alternating in the streamwise direction, as expected in the varicose scenario. This high-frequency disturbance is forcing a vertical motion which is disrupting the low-speed region (see also figure 13). Analysis of the velocity vectors shows similarities with what Jacobs & Durbin (2001) identified as the breakdown of backward jets.

The three-dimensional vortical structures observed in this case are displayed in figure 13. The black colour displays regions of negative values of the second largest eigenvalue λ_2 of the Hessian of the pressure (see Jeong *et al.* 1997), used to identify vortical structures, while the low- and high-speed streaks are shown in dark grey and

light grey, respectively, by considering negative and positive values of the streamwise velocity u' . The formation of a packet of vortical structures, characterized by pairs of counter-rotating quasi-streamwise vortices joining in the middle of the low-speed streak, can be seen in the figure. These structures point alternatively upstream and downstream and we will refer to them as V- and Λ -structures, respectively. It can also be seen that they are inclined away from the wall in the downstream direction.

It can also be deduced from figures 12 and 13 that the interaction between the low- and high-speed streak plays an important role in the formation of the incipient spot. This is not only true for the case considered here, but it is also evident from flow visualizations and animations of many of the considered spot precursors. The interaction of the low-speed streak with a fast-moving incoming region of high streamwise velocity is the triggering cause of the instability wave packet. It is observed in experiments (Lundell & Alfredsson 2004) that the streaks are tilted downstream so that the front part is located in the upper part of the boundary layer whereas the rear part is located closer to the wall. Such a structure is growing in the streamwise direction while convected downstream. As a consequence, highly inflectional wall-normal velocity profiles are induced by the high-speed region when reaching the tail of the low-speed region ahead, which thus becomes the site of a local instability.

The full velocity field corresponding to the structures observed is shown in figure 14, where the cross-stream velocities represented by velocity vectors and the streamwise component by constant levels in cross-stream (y, z)-planes cut along one wavelength of the streak varicose oscillation. The regions of strong vortical motions are also indicated by thick dashed lines. In figure 14(a), the downstream part of the head of the vortex pointing downstream (Λ -structure in figure 13) is seen to be located above the two legs of the V-structure pointing instead upstream. The legs of the latter correspond to quasi-streamwise vortices which slightly diverge downstream and induce negative wall-normal velocity in the middle of the low-speed streak (located at $z \approx -14$ for the particular spot precursor considered here) and positive wall-normal velocity on its sides. These streamwise vortices create two low-speed lumps in each period of the varicose oscillations (see figure 14a–c) in agreement with the streamwise velocity measurements of the varicose instability of a single steady streak in Asai *et al.* (2002). In figure 14(d), four vortical regions are visible: the downstream end of the V-structure and the upstream end of the Λ -structure. The legs of the latter also consist of quasi-streamwise vortices, which instead approach each other, and induce positive wall-normal velocity in the middle of the low-speed streak. In figure 14(f), we can see that the two legs join above the vertex of the following V-structure as in figure 14(a). By comparing figures 14(f) and 14(a), which corresponds to what is observed just downstream of figure 14(f), we can deduce that both the head of the Λ -structure and the vertex of the V-structure are associated with negative spanwise vorticity (positive v upstream and negative v downstream).

3.3.2. Sinuous-like breakdown

The time sequence showing the evolution of a typical sinuous-like breakdown scenario in a plane parallel to the wall ($y/\delta_0^* = 2.5$) is displayed in figure 15. It can be seen how a single low-speed streak (indicated by the dark background grey) undergoes spanwise antisymmetric oscillations, with strong high-frequency perturbation velocity located in the region of largest spanwise shear between the low- and high-speed streaks. The contour levels, showing the wall-normal velocity, highlight the growth of the unstable wave packet, while the area depicted in the plot is travelling downstream at speed $c = 0.7U_\infty$. The instantaneous three-dimensional flow field for this type of

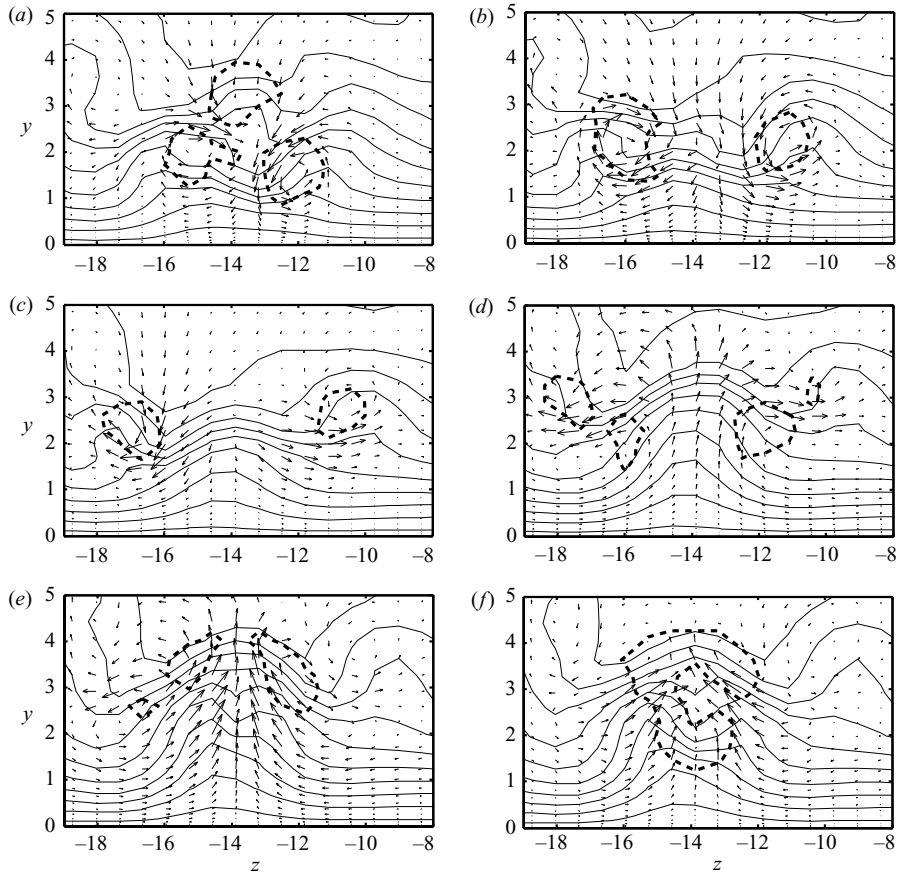


FIGURE 14. Vertical planes in the cross-stream directions showing details of the incipient spots depicted in figure 13. The arrows represent the spanwise and wall-normal velocities, while solid lines indicate constant streamwise velocity from 0.05 to 0.95 with spacing of 0.1. The thick dashed lines represent constant negative values of λ_2 and show the core of the vortical structures. (a) $x = 350$, (b) $x = 352$, (c) $x = 354$, (d) $x = 357$, (e) $x = 359$, (f) $x = 361$.

scenario is displayed in figure 16. The characteristic vortical structures, represented in black by negative values of the eigenvalue λ_2 , consist of quasi-streamwise vortices located on the flanks of the low-speed streak (depicted in dark grey). Vortices of alternating sign are overlapping in the streamwise direction in a staggered pattern.

The instantaneous flow in vertical planes at different streamwise positions, covering a distance corresponding to about one sinuous oscillation of the low-speed streak, is displayed in figure 17. The velocity vectors show the spanwise and wall-normal velocity. The isolines represent the streamwise velocity and the thick dashed lines regions of vortical motion. The evolution of two quasi-streamwise vortices, of opposite sign, is followed in the plots. In figures 17(a) and 17(b), we can see the vortex characterized by negative vorticity, located on the left-hand side of the low-speed streak, following the motion of the streak in the positive z -direction. Already in figure 17(b), the vortex with positive streamwise vorticity is visible. It follows the oscillation of the low-speed streak in the negative z -direction. The flow presents remarkable similarity with the structures observed in the simulations of the sinuous

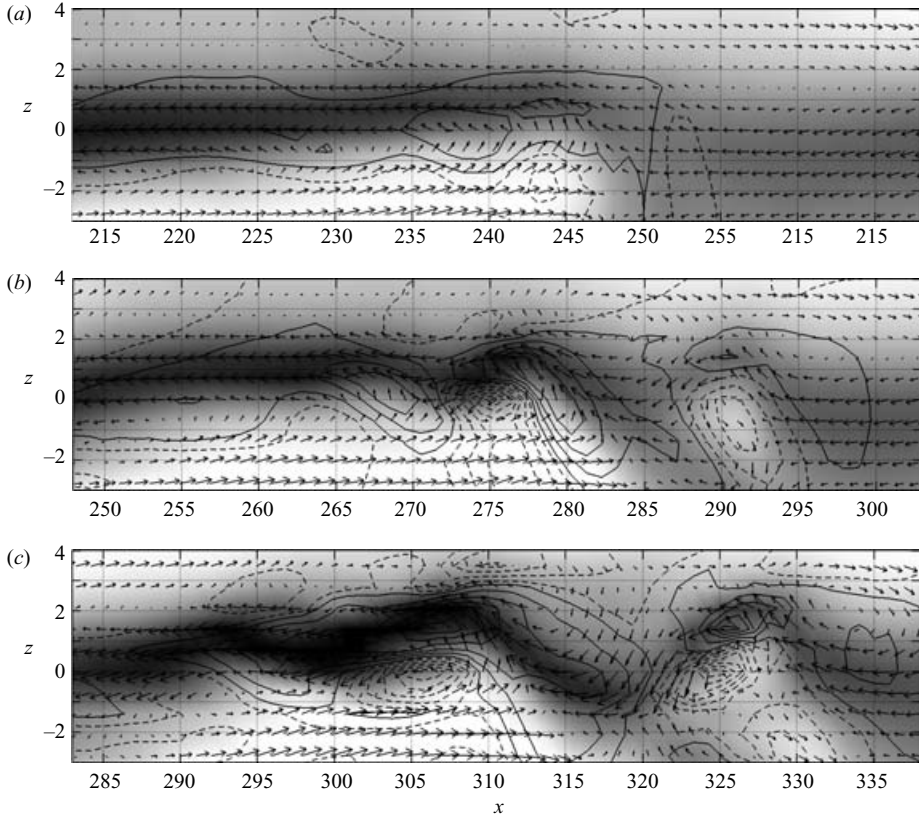


FIGURE 15. Time sequence showing the evolution of a typical sinuous-like breakdown in a plane parallel to the wall ($y/\delta_0^* = 2.5$). The velocity vectors represent the streamwise perturbation velocity u' and the spanwise velocity w . Black lines represent isocontours of wall-normal velocity of value $\pm 0.0075, \pm 0.0225, \pm 0.0375 \dots$ (dashed lines indicate the negative values). The background shows values of streamwise velocity u' from negative values (dark areas) to positive (light areas). From top to bottom $t'' = 0, 50, 100$. The displayed area moves at $c = 0.7U_\infty$ to maintain the perturbation in the picture. The range $x \in [210, 340]$ corresponds to $Re_x \in [0.94 \times 10^5, 1.32 \times 10^5]$ and the data are extracted from simulation Case4.

breakdown of a periodic array of streaks shown in figures 18 and 19 in Brandt & Henningson (2002).

It is also important to note that for about half of the incipient spots, which have been classified as sinuous-like breakdown, the quasi-streamwise vortices of either positive or negative vorticity dominate. This can be related to a spanwise asymmetry of some of the streaks generated by free-stream turbulence. An example of this 'one-side' instability is displayed in figure 18. It can be seen that the spanwise oscillations of the streak occur only in the negative z -direction. The high-frequency perturbations are centred in the region of largest spanwise shear on one side of the low-speed streak ($z \approx -2$ in the case in the figure) and reproduce patterns similar to those of one of the two vortices in figure 17. The lack of a region of significant positive streamwise velocity perturbation on the other side of the low-speed streak ($z \approx -6$) accounts for the differences with the case of the sinuous breakdown in figure 16. The observed breakdown can be considered the result of the instability of a spanwise velocity profile with an inflection point (and not two as in the case of symmetric streaks or wakes).

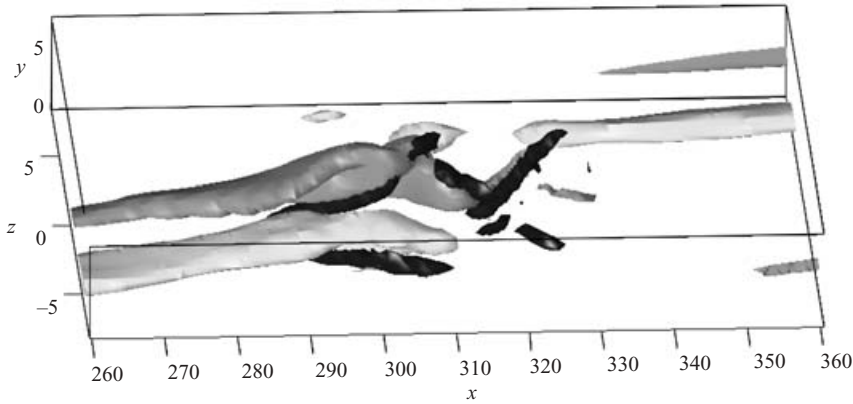


FIGURE 16. Instantaneous flow configuration at the sinuous-like breakdown of a streamwise streak. Light grey represents positive perturbation streamwise velocity ($u' = 0.14$), while dark grey indicates the low-speed streak ($u' = -0.14$). The black structures are regions of negative λ_2 , used to identify vortical structures. The range $x \in [260, 360]$ corresponds to $Re_x \in [1.08 \times 10^5, 1.38 \times 10^5]$ and the data are extracted from simulation Case4 at time $t'' = 92$ (see figure 15).

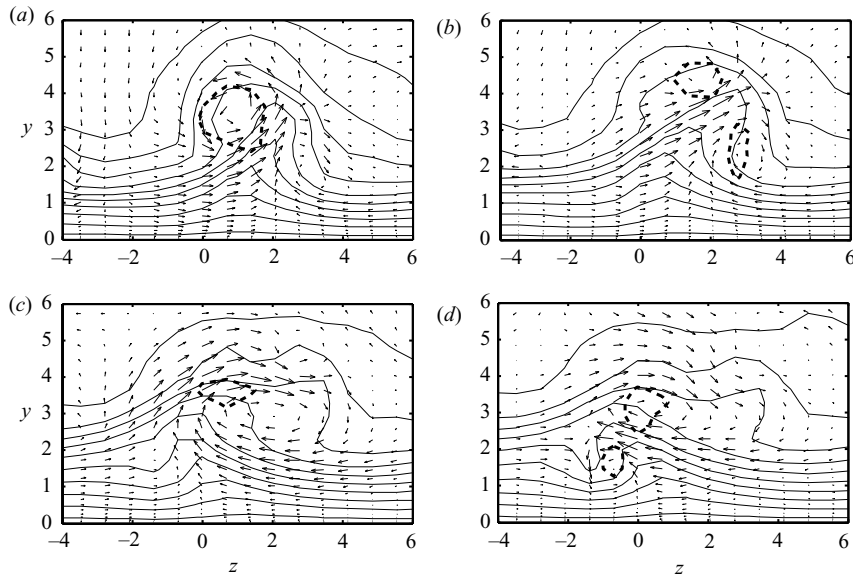


FIGURE 17. Vertical planes in the cross-stream directions showing details of the incipient spots depicted in figure 16. The arrows represent the spanwise and wall-normal velocities, while solid lines indicate constant streamwise velocity from 0.05 to 0.95 with spacing of 0.1. The thick dashed lines represent constant negative values of λ_2 and show the core of the vortical structures. (a) $x = 304$, (b) $x = 307$, (c) $x = 311$, (d) $x = 314$.

The sinuous-like scenario discussed in this section is also often initiated by the interactions between streaks; in particular, when high-speed fluid is approaching a low-speed region on one side. In this case, an inflectional profile is formed in the spanwise direction. This is observed for the case in figures 16 and 15 at $z \approx 0$ and $300 \lesssim x \lesssim 310$, and in figure 18 at $z \approx -1$ and $x \approx 355$. Note that the streaks are

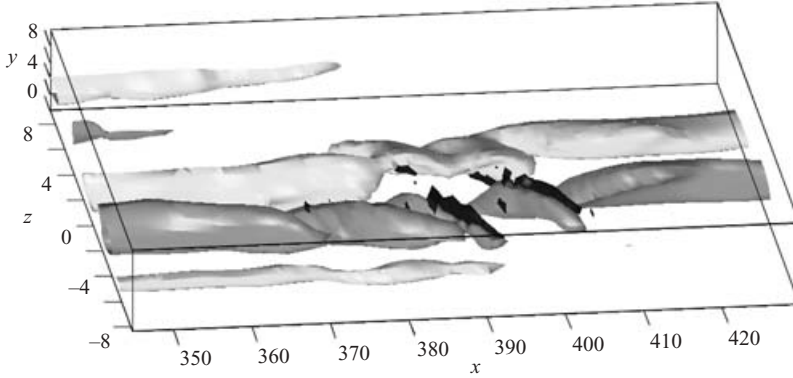


FIGURE 18. Instantaneous flow configuration at the breakdown of a streamwise streak for the case of the one-sided sinuous-like scenario. Light grey represents positive perturbation streamwise velocity ($u' = 0.12$), while dark grey indicates the low-speed streak ($u' = -0.12$). The black structures are regions of negative λ_2 , used to identify vortical structures. The range $x \in [345, 430]$ corresponds to $Re_x \in [1.34 \times 10^5, 1.6 \times 10^5]$ and the data are extracted from simulation Case4.

not perfectly aligned in the streamwise direction, but they slowly oscillate in the boundary layer. Once an unstable flow configuration is locally induced by the streak relative motion, high-frequency perturbations start to grow and disrupt the streak. These high-frequency modes are most probably induced by free-stream turbulence eddies. It can be seen in figures 14 and 17 that the regions of largest wall-normal and spanwise shear are located in the upper part of the boundary and they are, therefore, very receptive to perturbations coming from above.

Finally, it is interesting to notice that Asai *et al.* (2002) observed that wider streaks undergo more easily the varicose breakdown, while the sinuous scenario is most likely to occur with narrow streaks. The same seems to be true in the present case, as seen by comparing the width of the streaks in figures 17, 18 and 14. From the analysis of the secondary high-frequency oscillations, it can also be concluded that their typical wavelength is about $15\delta^*$; a clear distinction in wavelength between the two types of breakdown is not observed.

4. Summary and conclusions

Numerical simulations of bypass transition in a Blasius boundary layer subjected to free-stream turbulence have been performed. The present scenario is characterized by the formation of streamwise elongated regions of high and low streamwise velocity inside the boundary layer. The free-stream turbulence is generated by the superposition of modes of the continuous spectrum of the Orr–Sommerfeld and Squire operators. The numerical methodology implemented allows to us define the energy spectrum of the turbulent inflow, so that it has been possible to investigate the effect of the integral length scale of the free-stream turbulence and the receptivity process. Further, since laboratory experiments have not completely elucidated the mechanisms of formation of turbulent spots, the present study is also focused on the breakdown stage. The main findings can be summarized as follows.

Considering the same intensity of the incoming perturbation, transition occurs earlier for larger values of the integral length scale of the free-stream turbulence. It is also shown that the small scales can penetrate easier into the boundary layer

and therefore induce significant streamwise velocity perturbations at lower Reynolds number. However, the growth of the perturbation is not sustained for a long distance downstream as in the cases with larger integral length scales. Note also that the spanwise scale of the streaks is only weakly dependent on the scale of the disturbance in the free stream.

The energy spectrum of the turbulent inflow has been manipulated in order to control the amount of low-frequency disturbance present at the inlet. This enabled us to compare two possible receptivity mechanisms. A linear mechanism (Bertolotti 1997; Andersson *et al.* 1999; Luchini 2000) which requires the presence of streamwise vortices diffusing/propagating into the boundary layer mainly at the leading edge and a nonlinear process in which the streamwise vortices are induced by the interaction of oblique waves in the free stream (Berlin & Henningson 1999; Brandt *et al.* 2002). It is found that the linear mechanism is the most relevant if the free-stream turbulence contains low-frequency disturbances, whereas the nonlinear process is active if the free-stream turbulence mainly contains high-frequency disturbances.

It is observed that the breakdown into turbulent spots occurs on isolated streaks in the form of a growing wave packet and it is associated with high-frequency motions of the low-speed streak. The characteristic structures of the spot precursors are found to be very similar to those observed in previous model studies on the secondary instability and breakdown of steady symmetric streaks, both for the sinuous symmetry and for the varicose symmetry (see Asai *et al.* 2002, for a recent experimental investigation). From the results presented, we may conclude that the breakdown is related to local instabilities driven by the strong shear layers associated with the streaks, the sinuous-like breakdown being driven by the spanwise shear and the varicose-like breakdown by the wall-normal shear. Also note that the sinuous-like scenario is observed to be slightly more likely to occur. It is observed that in some cases, owing to the intrinsic asymmetry of the streaks induced by free-stream turbulence, a sinuous-like instability develops only on the side of the low-speed streak associated with the largest spanwise shear. The quasi-streamwise vortices and typical flow patterns reproduce well those observed during half a period of the sinuous oscillations of a symmetric streak.

The direct numerical simulations have also shown the importance of the relative motions between the low- and high-speed streaks, since the regions of strongest shear are mainly induced by streaks in relative motion. The relevance of such interactions was first suggested by Johansson, Alfredsson & Kim (1991) and Landahl (1990) for the case of near-wall turbulent streaks. Note that also Wu & Choudhari (2001) showed that the unsteadiness of the Klebanoff modes plays a crucial role. These authors found instability modes which would not have been present if streaks of the same amplitude were treated as steady.

It is also interesting to note that Schoppa & Hussain (2002) showed that steady streaks, stable to linear perturbations, can undergo a sinuous breakdown to turbulence if subjected to specific initial disturbances of sufficiently high amplitude. The breakdown is characterized by structures identical to those identified by Brandt & Henningson (2002) in the case, of a linearly unstable streak. We note that in the present case, the background level of noise is high enough to induce such subcritical breakdown. However, stability calculations of the streak profiles extracted from the numerical data have not been performed here.

Although transition occurs at Reynolds numbers above the critical value for exponential instabilities, Tollmien–Schlichting waves are not observed to affect the present scenario. Indeed, free-stream turbulence cannot generate such a travelling mode of significant amplitude without scattering from a surface roughness. Simulations might be

designed to introduce travelling modes artificially from the wall as in the experiments by Boiko *et al.* (1994). These authors observed that the linear amplification rate of the Tollmien–Schlichting waves evolving under free-stream turbulence is lower than in the undisturbed Blasius boundary layer; a result later confirmed for steady streaks by the simulations in Cossu & Brandt (2002). Boiko *et al.* (1994) noticed also that, when increasing the forcing amplitude, the presence of high-frequency waves inside the boundary layer leads to an increase in the number of turbulent spots.

One may also note the similarity between the near-wall streaks in turbulent boundary layers and their instability (Jiménez & Pinelli 1999; Schoppa & Hussain 2002) and the structure observed in transitional boundary layers. We can speculate that the near-wall streamwise vortices and streaks are driven by the turbulence in the outer part of the boundary layer in the same way that laminar streaks are induced by the free-stream turbulence. As a consequence, the receptivity stage becomes an important ingredient of the regeneration cycle of near-wall turbulence, together with the streak formation by the linear lift-up effect and the streak breakdown. This connection therefore deserves future work.

This research was supported by VR (The Swedish Research Council). Computer time was provided by the Center for Parallel Computers (PDC) at the Royal Institute of Technology (KTH) and by the National Supercomputer Center in Sweden (NSC) at Linköping University. The authors would like to thank Professor Henrik Alfredsson and Dr Fredrik Lundell for useful discussions. P. S. acknowledges financial support from the Swiss National Science Foundation and the Swiss Center of Scientific Computing (CSCS) during his visits in Stockholm.

REFERENCES

- ANDERSSON, P., BERGGREN, M. & HENNINGSON, D. S. 1999 Optimal disturbances and bypass transition in boundary layers. *Phys. Fluids* **11**, 134–150.
- ANDERSSON, P., BRANDT, L., BOTTARO, A. & HENNINGSON, D. S. 2001 On the breakdown of boundary layers streaks. *J. Fluid Mech.* **428**, 29–60.
- ARNAL, D. & JUILLEN, J. C. 1978 Contribution expérimentale à l'étude de la reptivité d'une couche limite laminaire à la turbulence de l'écoulement général. *Rapport Technique 1/5018*. ONERA.
- ASAI, M., MINAGAWA, M. & NISHIOKA, M. 2002 The instability and breakdown of a near-wall low-speed streak. *J. Fluid Mech.* **455**, 289–314.
- BERLIN, S. & HENNINGSON, D. S. 1999 A nonlinear mechanism for receptivity of free-stream disturbances. *Phys. Fluids* **11**, 3749–3760.
- BERTOLOTTI, F. P. 1997 Response of the Blasius boundary layer to free-stream vorticity. *Phys. Fluids* **9**, 2286–2299.
- BERTOLOTTI, F. P., HERBERT, T. & SPALART, P. R. 1992 Linear and nonlinear stability of the Blasius boundary layer. *J. Fluid Mech.* **242**, 441–474.
- BERTOLOTTI, F. P. & KENDALL, J. M. 1997 Response of the Blasius boundary layer to controlled free-stream vortices of axial form. *AIAA Paper 97–2018*.
- BOIKO, A. V., WESTIN, K. J. A., KLINGMANN, B. G. B., KOZLOV, V. V. & ALFREDSSON, P. H. 1994 Experiments in a boundary layer subjected to free stream turbulence. Part 2. The role of TS-waves in the transition process. *J. Fluid Mech.* **281**, 219–245.
- BOTTARO, A. & KLINGMANN, B. G. B. 1996 On the linear breakdown of Görtler vortices. *Eur. J. Mech. B/Fluids* **15**, 301–330.
- BRANDT, L., COSSU, C., CHOMAZ, J.-M., HUERRE, P. & HENNINGSON, D. S. 2003 On the convectively unstable nature of optimal streaks in boundary layers. *J. Fluid Mech.* **485**, 221–242.
- BRANDT, L. & HENNINGSON, D. S. 2002 Transition of streamwise streaks in zero-pressure-gradient boundary layers. *J. Fluid Mech.* **472**, 229–262.

- BRANDT, L., HENNINGSON, D. S. & PONZIANI, D. 2002 Weakly non-linear analysis of boundary layer receptivity to free-stream disturbances. *Phys. Fluids* **14**, 1426–1441.
- BUTLER, K. M. & FARRELL, B. F. 1992 Three-dimensional optimal perturbations in viscous shear flow. *Phys. Fluids A* **4**, 1637–1650.
- COSSU, C. & BRANDT, L. 2002 Stabilization of Tollmien–Schlichting waves by finite amplitude optimal streaks in the Blasius boundary layer. *Phys. Fluids* **14**, L57–L60.
- CRAIK, A. D. D. 1991 The continuous spectrum of the Orr–Sommerfeld equation: note on a paper of Grosch & Salwen. *J. Fluid Mech.* **226**, 565–571.
- DRYDEN, H. L. 1937 Air flow in the boundary layer near plate. *Rep.* 562. NACA.
- ELLINGSEN, T. & PALM, E. 1975 Stability of linear flow. *Phys. Fluids* **18**, 487–488.
- ELOFSSON, P. A., KAWAKAMI, M. & ALFREDSSON, P. H. 1999 Experiments on the stability of streamwise streaks in plane Poiseuille flow. *Phys. Fluids* **11**, 915–930.
- FRANSSON, J. H. M. 2003 Flow control of boundary layers and wakes. PhD thesis, Royal Institute of Technology, Stockholm, Sweden.
- FRANSSON, J. H. M., MATSUBARA, M. & ALFREDSSON, P. H. 2004 Transition induced by free stream turbulence. *J. Fluid Mech.* Submitted.
- GOLDSTEIN, M. E. & WUNDROW, D. W. 1998 On the environmental realizability of algebraically growing disturbances and their relation to Klebanoff modes. *Theor. Comput. Fluid Dyn.* **10**, 171–186.
- GROSCHE, C. E. & SALWEN, H. 1978 The continuous spectrum of the Orr–Sommerfeld equation. Part 1. The spectrum and the eigenfunctions. *J. Fluid Mech.* **87**, 33–54.
- HALL, P. & HORSEMAN, N. J. 1991 The linear inviscid secondary instability of longitudinal vortex structures in boundary layers. *J. Fluid Mech.* **232**, 357–375.
- HENNINGSON, D. S., LUNDBLADH, A. & JOHANSSON, A. V. 1993 A mechanism for bypass transition from localized disturbances in wall-bounded shear flows. *J. Fluid Mech.* **250**, 169–207.
- HERBERT, T. & LIN, N. 1993 Studies of boundary-layer receptivity with parabolized stability equations. *AIAA Paper* 93-3053.
- HULTGREN, L. S. & GUSTAVSSON, L. H. 1981 Algebraic growth of disturbances in a laminar boundary layer. *Phys. Fluids* **24**, 1000–1004.
- JACOBS, R. G. & DURBIN, P. A. 1998 Shear sheltering and the continuous spectrum of the Orr–Sommerfeld equation. *Phys. Fluids* **10**, 2006–2011.
- JACOBS, R. G. & DURBIN, P. A. 2001 Simulations of bypass transition. *J. Fluid Mech.* **428**, 185–212.
- JEONG, J., HUSSAIN, F., SCHOPPA, W. & KIM, J. 1997 Coherent structures near the wall in a turbulent channel flow. *J. Fluid Mech.* **332**, 185–214.
- JIMÉNEZ, J. & PINELLI, A. 1999 The autonomous cycle of near wall turbulence. *J. Fluid Mech.* **389**, 335–359.
- JOHANSSON, A. V., ALFREDSSON, P. H. & KIM, J. 1991 Evolution and dynamics of shear-layer structures in near-wall turbulence. *J. Fluid Mech.* **224**, 579–599.
- JONÁŠ, P., MAZUR, O. & URUBA, V. 2000 On the receptivity of the by-pass transition to the length scale of the outer stream turbulence. *Eur. J. Mech. B/Fluids* **19**, 707–722.
- KENDALL, J. M. 1985 Experimental study of disturbances produced in a pre-transitional laminar boundary layer by weak free-stream turbulence. *AIAA Paper* 85-1695.
- KENDALL, J. M. 1998 Experiments on boundary layer receptivity to free-stream turbulence. *AIAA Paper* 98-0530.
- KLEBANOFF, P. S. 1971 Effect of free-stream turbulence on the laminar boundary layer. *Bull. Am. Phys. Soc.* **10**, 1323.
- LANDAHL, M. T. 1975 Wave breakdown and turbulence. *SIAM J. Appl. Maths* **28**, 735–756.
- LANDAHL, M. T. 1980 A note on an algebraic instability of inviscid parallel shear flows. *J. Fluid Mech.* **98**, 243–251.
- LANDAHL, M. T. 1990 On sublayer streaks. *J. Fluid Mech.* **212**, 593–614.
- LUCHINI, P. 2000 Reynolds-number independent instability of the boundary layer over a flat surface. Part 2. Optimal perturbations. *J. Fluid Mech.* **404**, 289–309.
- LUNDBLADH, A., BERLIN, S., SKOTE, M., HILDINGS, C., CHOI, J., KIM, J. & HENNINGSON, D. S. 1999 An efficient spectral method for simulation of incompressible flow over a flat plate. *Tech. Rep.* KTH/MEK/TR-99/11-SE. KTH, Department of Mechanics, Stockholm.
- LUNDELL, F. & ALFREDSSON, P. H. 2004 Streamwise scaling of streaks in laminar boundary layers subjected to free-stream turbulence. *Phys. Fluids* **16**, 1814–1817.

- MATSUBARA, M. & ALFREDSSON, P. H. 2001 Disturbance growth in boundary layers subjected to free stream turbulence. *J. Fluid Mech.* **430**, 149–168.
- MATSUBARA, M., BAKCHINOV, A. A., FRANSSON, J. H. M. & ALFREDSSON, P. H. 2000 Growth and breakdown of streaky structures in boundary layer transition induced by free stream turbulence. In *Proc. IUTAM Symp., Sedona/AZ 1999* (ed. H. F. Fasel & W. S. Saric), pp. 371–376. Springer.
- PARK, D. S. & HUERRE, P. 1995 Primary and secondary instabilities of the asymptotic suction boundary layer on a curved plate. *J. Fluid Mech.* **283**, 249–272.
- PHILLIPS, O. M. 1969 Shear-flow turbulence. *Annu. Rev. Fluid Mech.* **1**, 245–264.
- RAI, M. M. & MOIN, P. 1993 Direct numerical simulation of transition and turbulence in a spatially evolving boundary layer. *J. Comput. Phys.* **109**, 169–192.
- REDDY, S. C. & HENNINGSON, D. S. 1993 Energy growth in viscous channel flows. *J. Fluid Mech.* **252**, 209–238.
- REDDY, S. C., SCHMID, P. J., BAGGETT, J. S. & HENNINGSON, D. S. 1998 On the stability of streamwise streaks and transition thresholds in plane channel flows. *J. Fluid Mech.* **365**, 269–303.
- ROACH, P. E. & BRIERLEY, D. H. 1990 The influence of a turbulent freestream on zero pressure gradient transitional boundary layer development, part I: Test Cases T3A and T3B. In *Numerical Simulation of Unsteady Flows and Transition to Turbulence* (ed. O. Pironneau, W. Rodi, I. L. Ryhming, A. M. Savill & T. V. Truong), pp. 319–347. Cambridge University Press.
- ROGALLO, R. S. 1981 Numerical experiments in homogeneous turbulence. TM 81315. NASA.
- SARIC, W. S., REED, H. L. & KERSCHEN, E. J. 2002 Boundary-layer receptivity to freestream disturbances. *Annu. Rev. Fluid Mech.* **34**, 291–319.
- SCHLATTER, P. 2001 Direct numerical simulation of laminar–turbulent transition in boundary layer subject to free-stream turbulence. *Tech. Rep.* Department of Mechanics, KTH Stockholm, also *Tech. Rep.*, Institute of Fluid Dynamics, ETH Zürich, 2001.
- SCHMID, P. J. & HENNINGSON, D. S. 2001 *Stability and Transition in Shear Flows*. Springer.
- SCHOPPA, W. & HUSSAIN, F. 2002 Coherent structure generation in near-wall turbulence. *J. Fluid Mech.* **453**, 57–108.
- SKOTE, M., HARITONIDIS, J. H. & HENNINGSON, D. S. 2002 Varicose instabilities in turbulent boundary layers. *Phys. Fluids* **14**, 2309–2323.
- SWEARINGEN, J. D. & BLACKWELDER, R. F. 1987 The growth and breakdown of streamwise vortices in the presence of a wall. *J. Fluid Mech.* **182**, 255–290.
- TAYLOR, G. I. 1939 Some recent developments in the study of turbulence. In *Proc. 5th Intl Congr. Appl. Mech.* (ed. J. Hartog & H. Peters), pp. 294–310. Wiley.
- TENNEKES, H. & LUMLEY, J. L. 1972 *A First Course in Turbulence*. MIT Press.
- WALEFFE, F. 1995 Hydrodynamic stability and turbulence: beyond transients to a self-sustaining process. *Stud. Appl. Maths.* **95**, 319–343.
- WALEFFE, F. 1997 On a self-sustaining process in shear flows. *Phys. Fluids* **9**, 883–900.
- WESTIN, K. J. A., BAKCHINOV, A. A., KOZLOV, V. V. & ALFREDSSON, P. H. 1998 Experiments on localized disturbances in a flat plate boundary layer. Part 1: the receptivity and evolution of a localized free stream disturbance. *Eur. J. Mech. B/Fluids* **17**, 823–846.
- WESTIN, K. J. A., BOIKO, A. V., KLINGMANN, B. G. B., KOZLOV, V. V. & ALFREDSSON, P. H. 1994 Experiments in a boundary layer subject to free-stream turbulence. Part 1. Boundary layer structure and receptivity. *J. Fluid Mech.* **281**, 193–218.
- WU, X. & CHOUDHARI, M. 2001 Linear and nonlinear instabilities of Blasius boundary layer perturbed by streamwise vortices. part II: Intermittent instability induced by long-wavelength Klebanoff modes. *Rep.* 2001-45. ICASE.
- WU, X., JACOBS, R. G., HUNT, J. C. R. & DURBIN, P. A. 1999 Simulation of boundary layer transition induced by periodically passing wakes. *J. Fluid Mech.* **398**, 109–153.
- WUNDROW, D. W. & GOLDSTEIN, M. E. 2001 Effect on a laminar boundary layer of small-amplitude streamwise vorticity in the upstream flow. *J. Fluid Mech.* **426**, 229–262.
- YANG, Z. & VOKE, P. 1995 Numerical study of bypass transition. *Phys. Fluids* **7**, 2256–2264.